Temporal Clonal Tracing and Functional Perturbation Reveal Niche-Adaptive and Tumor-Intrinsic IFNγ Dependencies Driving Ovarian Cancer Metastasis

Emilija Aleksandrovic[1,3], Shaneann R. Fross[1,3], Samantha M. Golomb[1,3], Xiyu Liu[1,3], Zhuo Zhao[2,3], Nikitha M. Das[1,3], Tanner C. Reese[1,3], Wei Ma[1,3], Jacqueline Lopez[4], M. Sharon Stack[5,6], Min Zhao[1,3], Siyuan Zhang[1, 3]

Affiliations:

1. Department of Pathology, UT Southwestern Medical Center, Dallas, TX, 75390, USA
2. Lyda Hill Department of Bioinformatics, School of Public Health, UT Southwestern Medical Center, Dallas, TX, 75390, USA
3. Harold C. Simmons Comprehensive Cancer Center, Dallas, TX, 75390, USA
4. Department of Biological Sciences, College of Science, University of Notre Dame, Notre Dame, IN 46556, USA
5. Department of Chemistry and Biochemistry, University of Notre Dame, Notre Dame, IN 46556, USA
6. Mike and Josie Harper Cancer Research Institute, University of Notre Dame, 1234 N. Notre Dame Avenue, South Bend, IN 46617, USA

*** Correspondence to:** Siyuan Zhang, M.D., Ph.D., Department of Pathology, UT Southwestern Medical Center, ND6.200A, 6001 Forest Park Rd., Dallas, TX 75235. E-mail: Siyuan.Zhang@UTSouthwestern.edu; Telephone: 214-648-6537

Key Words: Metastasis, Single cell analysis, Barcoding, Lineage tracing, CRISPR screening, Interferon, Ovarian Cancer, Omentum, Ascites.

SUMMARY

Metastasis is an emergent continuum, driven by evolving reciprocal adaptations between continuously disseminating tumor cells (DTCs) and the specialized metastatic niches of distant organs. The interplay between intrinsic and niche-driven mechanisms that enables DTCs to survive and home to distant organs remains incompletely understood. Here, using MetTag, a single-cell barcoding and transcriptome profiling approach with time-stamped batch identifiers (BC.IDs), we mapped temporal, clonal dynamics of DTCs and the immune cell landscape across ovarian cancer metastatic niches. Deep sequencing of barcodes revealed preferred enrichment of early-disseminated clones across metastatic niches. Mechanistically, single-cell RNA sequencing (scRNA-seq) coupled with velocity analyses in ascites and metastasis-bearing omenta uncovered an emergent, distinct interferon-gamma (IFNγ) centric transcriptional trajectory, enriched among early seeding clones. Moreover, *in vivo* CRISPR/Cas9 screening of metastatic niche-specific signatures demonstrated that genes belonging to the ascites IFNγ signature, including *Marco*, *Gbp2b, and Slfn1,* are functionally important for peritoneal metastasis. Knockout of IFNγ receptor 1 (*Ifngr1*) in tumor cells significantly reduced metastatic burden and extended survival, underscoring the importance of tumor cell intrinsic IFNγ signaling in ovarian cancer metastasis. Furthermore, we identified that the tumor intrinsic IFNγ response and ascites-derived tumor-associated macrophages (TAMs) protect cancer cells from anoikis-mediated death within the IFNγ-rich ascites environment. Our study resolves temporal dynamics of disseminating tumor cells and highlights an ascites-driven, IFNγ program as a necessary pro-metastatic adaptation in the ovarian metastasis cascade.

INTRODUCTION

Cancer metastasis encompasses continuous metastatic dissemination from the primary tumor, followed by passive clonal selection, and active epigenetic niche adaptation in response to the metastatic niche[1]. Unlike most cancer types, where hematogenous metastasis is common, high-grade serous ovarian carcinoma (HGSOC) exhibits a unique form of transcoelomic, local spreading within the peritoneal cavity[2]. In HGSOC,

detached cancer cells from the fallopian tube are carried by the physiological flow of peritoneal fluid to implant into intraperitoneal tissue, particularly into the omentum[3]. This unique mode of metastatic dissemination leads to continuous and widespread intraperitoneal metastases in the peritoneal cavity before colonizing distant organs[3]. Resolving the clonal, temporal, and microenvironmental determinants along the ovarian cancer metastatic continuum has long been a challenge in the field.

Malignant ascites formed in HGSOC patients is a known “reservoir” of floating cancer cells and cell clusters that can seed the omentum or other organs in the peritoneal cavity[4,5]. Aside from cancer cells, malignant ascites contains immune cells and acellular factors that influence pro-metastatic programs[6]. Notably, malignant ascites are enriched in pro-metastatic cytokines, which increase cancer cell migration and correlate with reduced disease-free progression[7,8]. In ascites, after shedding from the primary tumor, ovarian cancer cells acquire resistance to anoikis, a critical mechanism for surviving loss of attachment and enabling spread to other organs[9]. A key knowledge gap remains in how cellular and acellular factors in malignant ascites regulate anoikis resistance and shape the timing of successful colonization of intraperitoneal compartments.

Here, we conducted comprehensive lineage tracing, single-cell RNA sequencing (scRNA-seq), *in vivo* CRISPR screening, and Cre-based niche-tracing analysis to dissect the complex interplay between continuously arriving DTCs and ovarian metastatic niche microenvironments. We identified that early DTCs in ascites are dependent on niche-adaptive IFNγ response genes for omental colonization. We additionally found that the interferon-rich ascites microenvironment harbors a macrophage population capable of protecting cancer cells from anoikis-mediated death via direct contact. Together, our data provide novel insights into the temporal dynamics of ovarian cancer clonal dynamics and highlight ascites-specific factors that prime cancer cells for successful omental colonization.

RESULTS

MetTag Captures Clonal Lineage Across Metastatic Sites and Across Time

To capture the transcriptional dynamics across ovarian cancer metastasis, we employed an RNA-level barcoding system based on the LARRY (**L**ineage **A**nd **R**NA **R**ecover**y**) barcoding construct, enabling single-cell transcriptome-level lineage tracing[10]. In brief, we subcloned the publicly available highly diverse LARRY library downstream of a U6 promoter in a CROP-seq backbone. We next added a unique batch identifier "BC.ID" to the LARRY barcode for distinguishing early from later-arriving DTCs. In our "MetTag" system, early DTCs refer to the first two BC.ID batches and late DTCs represent the last two DTC batches. Individually barcoded and BC.ID batch-coded cells were later injected across six different time points to model early, mid, and late DTCs. Within the LARRY transcript, a Chromium 10x capture sequence allows for simultaneous capture of the LARRY transcript with mRNA transcripts (**Fig.1A, S1A**). Diversity of each BC.ID library batch was confirmed by deep next-generation sequencing (NGS). We observed a relatively consistent diversity across the six BC.ID library batches comparable with the original depositor LARRY library (**Fig.S1B-D**).

Next, we generated six unique isogenic ID8 p53$^{-/-}$ murine ovarian cancer pools (BC.ID1-6) with MetTag-LARRY-GFP lentiviral libraries harboring BC.IDs (**Fig.1A**). To model continuous seeding from the primary tumor, transduced cells were IP injected in a fractionated manner at low doses. The injections were separated by 48 hours to allow immune and stromal responses to occur after exposure to each DTC batch (**Fig.1B**). Four weeks after the final DTC exposure, ascitic fluid (Asc), omenta (Om), and peritoneal fat pads (FPs) were extracted. These organs and compartments consistently developed metastatic foci (**Fig.S1E**). This experimental scheme was performed under several immune cell depletion conditions, including wild type C57BL/6J (WT) mice, immunocompromised NOD.Cg-Rag1^{tm1Mom}IL2rg^{tm1Wjl}/SzJ (NRG) mice (lacking functional T, B, and NK cells), and under conditions of macrophage depletion via chlodrosome administration. Temporally spaced DTC exposure resulted in robust metastasis formation in fully immunocompetent mice, evidenced by ascites accumulation and positive GFP signal in the omentum and peritoneal adipose tissue (**Fig.S1E top**). After grouping BC.IDs into early timepoint "TP" (*BC.ID1, BC.ID2*), mid

120 (*BC.ID3, BC.ID4*), and late (*BC.ID5, BC.ID6*) arrivers, most BC.IDs detected using
121 amplicon DNA sequencing represent the early timepoint fraction (**Fig.1C-E**). These
122 results are consistent with clinical studies indicating that early cancer cell dissemination
123 is a common occurrence in ovarian and breast cancer metastasis [11–14]. Moreover, the
124 same tumor cell dosing and injection schema yielded reduced frequencies of GFP+
125 cancer cells in ascites fluids in macrophage-depleted mice compared with WT
126 C57BL/6J mice, indicating lower metastatic burden (**Fig.S1G**), suggesting an expected
127 role of the immune system in promoting metastasis. Interestingly, despite decreased
128 metastases burden, amplicon DNA sequencing revealed a near identical BC.ID
129 distribution across all three anatomical locations in both wild type and NRG mice
130 (**Fig.1C-1E**), as well as chlodrosome depletion in omenta (**Fig.1C**), suggesting a
131 negligible role of niche-specific tumor immune microenvironment (TIME) in the overall
132 dominance of early arriving DTCs.
133
134 To understand if later-arriving cancer cells are dispensable for overall metastases
135 burden, we evaluated tumor burden in mice with a single injection of tumor cells (TP-1
136 only) compared to mice with fractionated dosing (TP1-6) as described in Fig.1B in WT
137 mice with luciferase-tagged ID8 p53$^{-/-}$ cells. At the experimental endpoint of 4 weeks
138 post final cancer cell injection, tumor burden levels were comparable (**Fig.1F-G**),
139 measured by *in vivo* bioluminescent imaging (BLI). This indicates that early DTCs are
140 not dependent on later DTCs for metastatic colonization and outgrowth. Given that the
141 disseminating ID8 p53$^{-/-}$ cancer cells are isogenic and have the same genomic
142 alterations in each batch, this preliminary data strongly suggests that early DTC survival
143 could be attributed to transcriptional adaptations facilitating increased fitness in a niche-
144 specific manner.
145
146 To gain a better understanding of the transcriptional programs necessary for early DTCs
147 to colonize and subsequently assess their clonal expansion status, we performed CITE-
148 seq (scRNA-seq with HTO sample multiplexing) coupled with direct capture of U6-driven
149 MetTag transcripts via capture sequence 1 (CS1) (**Fig. 1H**). Sequential injections were
150 performed in the same manner as in Fig.1B with a reverse barcode injection schema to

151 ensure no unintended bias towards certain barcodes gained over the cell selection
152 period. Single cell analysis of MetTag BC.IDs of metastasis-bearing tissues showed that
153 early DTCs (*TP1-2*) were enriched in overt metastases (**Fig.1H-I**), consistent with gDNA
154 sequencing data in Fig. 1C and 1D. Moreover, integrated analysis of ascites and
155 omentum single-cell datasets showed a prominent trend towards early DTC dominance,
156 especially in ascites (**Fig.1I-J**). Differential gene expression (DEG) analysis between
157 early and late timepoint cancer cells confirmed that early DTC "TP-1" cells adopted
158 unique transcriptional programs (**Fig. 1K**). Notably, the top enriched gene in TP-1 cells,
159 small nucleolar RNA host gene 18 (Snhg18), is a lncRNA with known roles in
160 modulating expression of genes involved in invasion and cell proliferation[15,16].
161
162 **Clonal Transcriptomics Analysis of DTCs Reveals Shared Evolutionary Path**
163 **Towards Inflammatory Signature**
164 To further investigate characteristics of early and late DTCs, we assessed whether
165 clonal dynamics differed between niches. Specifically, as most DTCs do not survive and
166 only rare clones successfully adapt to metastatic niches[17], we asked whether tumor
167 cells disseminated over time evolve along diverse trajectories or adopt a convergent
168 path leading to symptomatic overt metastases. To explore this, we performed a deeper
169 analysis on the cancer cell compartment, integrating clonal barcode information with
170 transcriptional profiles across ascites and omental niches. We first annotated cell
171 clusters with higher levels of keratins and absence of CD45 transcript expression
172 (*Krt18*+, *Krt8*+, *Ptprc*-) as the tumor cell-enriched cluster on the Seurat[18] UMAP (**Fig. 2A**
173 **and S2A**). After reclustering *Krt18*+/*Krt8*+/*Ptprc*- cells, cell cluster states were
174 determined through a combination of cluster marker genes and pathway-level analysis
175 using the Escape R package[19] (**Fig. S2B – S2E**). Ascites-derived cancer cells (AscMet)
176 displayed distinct transcriptional states from those in the omentum (OmMet) (**Fig. 2B-**
177 **2D**). Single Cell Gene Set Enrichment Analysis (ssGSEA) further showed that ascites-
178 derived cells were strongly enriched for interferon alpha (IFNα) and gamma (IFNγ)
179 signaling, as opposed to more heterogeneous pathways enriched in the metastatic
180 omentum (**Fig. 2E**). OmMet consisted of 4 distinct subclusters/modules: proliferative,

181 epithelial-mesenchymal transitioning (EMT), matrisome, and a hypoxic, inflammatory
182 subcluster (**Fig. 2D-2E**).
183
184 Cellular barcoding approaches have been widely used to reveal clonal dynamics driven
185 by both genetic predisposition and epigenetic changes in response to environmental
186 cues[20]. Integrating LARRY BC with single-cell transcriptome readouts, we asked
187 whether the most expanded clones would 1) cluster together based on transcriptional
188 status, suggesting genetically pre-determined cell-autonomous programs that drive
189 ovarian cancer metastasis; 2) occupy heterogeneous transcriptional states (clusters),
190 indicating diverse transcriptional adaptation to different metastatic niche-derived cues
191 (**Fig. 2F**). Interestingly, we observed minimal overlap between dominant clones across
192 each HTO/mouse in both anatomical locations (**Fig. 2G**) - while one clone, BC-1, was
193 shared across ascites and omentum, the most of highly expanded clones are distinct
194 between metastatic niches. These results suggest that successful clonal outgrowth
195 requires unique adaptations reflective of the specific microenvironment.
196
197 Given that omentum metastases showed diverse single cell transcriptional states (**Fig.**
198 **2D-E**), we projected clonal identity of the most expanded clones from the omentum onto
199 the cancer cell UMAP and examined similarities between clones. At both the
200 transcriptome cluster and pathway levels, dominant clones were enriched for several
201 defined signatures (**Fig. 2H-2I, S2F**). Apart from the proliferative subcluster 4, expanded
202 clones consistently occupied the hypoxic, inflammatory subcluster 0 (**Fig. 2I**),
203 suggesting diverse, yet directed evolutionary trajectories within the same clonal lineage.
204 To understand the lineage relationships among different subclusters, we applied RNA
205 velocity and pseudotime analysis using scVelo and CellRank[21]. Paga velocity and
206 pseudotime analyses revealed a clear trajectory originating from the “primitive” ascites
207 compartment subcluster 3, leading to proliferative status, then further converging to
208 subcluster 0, a terminal inflammatory state in the omentum (**Fig. 2J & 2K, Fig. S2G**).
209 Notably, IFNγ, but not the IFNα signature, was significantly enriched in early DTCs (**Fig.**
210 **2L, S2H**). Together, the integrated clonal and transcriptional analysis suggests that
211 successful metastatic clones occupy several niche-dependent transcriptional states.

212 These evolved phenotypes appear to originate from the ascites compartment, which
213 encompasses an IFN-signaling-rich module that may prime these later adaptations.
214
215 ***In vivo* CRISPR screen identifies functional essentiality of IFNγ signaling in**
216 **omental colonization**
217 As ovarian cancer cells initially disseminate into the peritoneal cavity to form ascites, we
218 next asked whether transcriptional adaptation of cancer cells to the ascites environment
219 is essential for subsequent intraperitoneal seeding and successful omental metastasis.
220 Here, we hypothesized that the ascites gene signature adopted by early DTCs –
221 characterized by limited nutrient availability and low attachment – is (1) induced by initial
222 detachment from a primary tumor and (2) necessary for subsequent peritoneal
223 metastasis. To test this hypothesis, we performed differential gene expression (DEG)
224 analysis and over-representation pathway analysis (ORA) with the clusterProfiler R
225 package[22] to compare gene expression in metastatic tumor cells residing in the two
226 distinct niche compartments (Asc vs Om). Compared to OmMet, DEGs of AscMet were
227 enriched in hemoglobin genes (*Hbb-bs, Hba-a1, Hba-a2, Hbb-bt*) and interferon-
228 stimulated genes (*Ifi27l2a* and *Irf7*). In contrast, OmMets were enriched in immediate-
229 early response genes (*Atf3, Egr1, Fos, Fosb, Jun*)[23,24], adaptive immune
230 immunoglobulin components (*Igkc, Igha, Jchain*)[25], and angiogenesis (*Vegfa*) (**Fig. 3A**).
231 Next, IFNγ/IFNα module scoring and ORA analysis confirmed a dominant interferon-rich
232 inflammatory signature in AscMet, as opposed to more heterogeneous programs in
233 OmMet (**Fig. 3B, Fig. S3A & B**).
234
235 To assess the functional significance of AscMet-OmMet DEGs, we designed a custom *in*
236 *vivo* CRISPR/Cas9 screen targeting 100 DEGs identified (**Fig. 3C,** "In Vivo Ovarian
237 Metastatic Niche Signature Screen"). We introduced SpCas9 into ID8 p53$^{-/-}$ ovarian
238 cancer cells via PiggyBac (PB) transposon system and validated Cas9 expression (**Fig.**
239 **S3C**). Cas9 function was validated by assessing loss of mCherry fluorescence over 5
240 days, after transfection of sgRNA targeting mCherry (**Fig. S3D**). After constructing the
241 curated sgRNA library containing 1,030 different guides, ID8.Cas9 cells were
242 transduced at an MOI of 0.15. After 7 days of puromycin selection, 2.4 million cells

243 (~2000X representation of sgRNA library) were i.p. injected to a whole-body Cas9-
244 expressing host (Rosa26-Cas9 knockin on B6J, Jax 026179) (**Fig. 3C**). This host has
245 central tolerance to Cas9, decreasing immunogenicity towards Cas9-expressing tumor
246 cells[26]. Six weeks post-injection, metastasis-bearing omenta and ascites were
247 harvested for genomic DNA (gDNA) extraction and NGS sequencing, followed by
248 MAGeCK[27] analysis (**Fig. 3C**). The positive controls for the screen, *Pten* sgRNAs, were
249 significantly enriched in metastases derived from both anatomical locations (**Fig. 3D &**
250 **3E**). Compared to the initial injected cell pool sgRNA distribution, sgRNAs targeting
251 eight genes in OmMet and ten genes in AscMet were significantly depleted ($p < 0.05$)
252 (**Fig. 3D**). These results were further visualized by plotting the distribution of each
253 sgRNA for top hits (**Fig. 3E**). The top depleted (dropout) genes – *CD300lb*, *Ms4a8a*,
254 *Marco*, *Gbp2b* (OmMet), and *Slfn1* (AscMet) – were all upregulated DEGs identified in
255 AscMet, suggesting a necessity for transcriptome adaptation to the ascites niche - the
256 first niche DTCs encounter - for ultimate metastasis success. Furthermore, GSEA
257 analysis of dropout genes using the GO Biological Function (GOBP) gene sets revealed
258 a shared enrichment of apoptotic cell clearance processes in both Asc and Om
259 compartments and enrichments of programs related to interferon−gamma and
260 interleukin−1 response (**Fig. 3F**). Despite high IFNγ signaling in AscMet which was
261 described in Fig.2 and Fig.3B, OmMet expressed a higher level of *Ifngr1* compared to
262 AscMet (**Fig. S3E**), consistent with IFNγ response dependency observed in the *in vivo*
263 CRISPR screen (**Fig. 3F**). These data suggest that, despite the heterogeneity of
264 transcriptional programs revealed by scRNA-seq, the (1) shared essentiality of apoptotic
265 pathway regulation across ascites and omentum, and (2) IFNγ response first activated
266 in ascites, later necessary for omental metastasis, are both critical DTC adaptive
267 cellular processes that collectively drive ovarian metastases.
268

269 **Loss of IFNγ-response in DTCs significantly decreases peritoneal metastases and**
270 **extends overall survival**

271 To experimentally validate IFN-γ inducibility of screen hits in cancer cells, we treated ID8
272 p53$^{-/-}$ cells *in vitro* with recombinant IFN-γ and tested the inducibility of *Marco*, *Gbp2b*,
273 and *Slfn1* via RT-qPCR, where *Stat1* and *Irf1* transcription factors served as positive

274 controls for IFN-γ response[28] (**Fig. 3G**). By 24 hours of treatment, all three genes
275 displayed significant IFN-γ inducibility (**Fig. 3G**). *Gbp2b* (*GBP1* gene in humans) is an
276 interferon-inducible GTPase and part of the large guanylate-binding protein (GBP)
277 family with known roles in innate immune cells such as promoting antimicrobial
278 immunity, inflammatory response, and cell death regulation[29]. Although this protein was
279 shown to have both pro- and anti-tumor effects in various cancer contexts, in ovarian
280 cancer high Gbp2b expression mediates chemotherapy resistance[30,31]. With Gbp2b
281 being the most statistically significant hit in the screen, we also validated its inducibility
282 on the protein level via Western Blot (**Fig. 3H**).
283
284 Given that the top hits from the CRISPR screen were IFNγ-inducible, we reasoned that
285 IFNγ may serve as a primary regulator that exerts broader pro-metastatic adaptive
286 cellular programs in DTCs. Thus, instead of focusing on a single downstream gene
287 target, we sought to disable the entire cascade. To assess the functional role of the IFNγ
288 signaling pathway in tumor cells during ovarian cancer metastasis, we genetically
289 knocked out the IFNγ receptor 1, *Ifngr1,* in ID8 p53$^{-/-}$ cells. Successful knockout of *Ifngr1*
290 was validated via flow cytometry (**Fig. S3F**) and ablation of the IFN-γ transcriptional
291 downstream targets was validated via western blot probing for Stat1 and Gbp2b (**Fig.
292 S3G**). We next I.P. injected Cas9-expressing mice with either ID8.Luciferase-sgNTC or
293 ID8.Luciferase-sgIfngr1. Tumor burden was monitored by BLI intensity throughout the 6-
294 week experimental window (**Fig. 3I**). sgIfngr1 groups showed a significant reduction of
295 overall metastasis burden compared with sgNTC group (**Fig. 3J**). In contrast to sgNTC
296 group, ~80% of mice in the sgIfngr1 groups remained alive at the end of the survival
297 study (**Fig. 3K**). Furthermore, in human ovarian cancer microarray gene expression
298 data[32], patients with ovarian cancer expressing lower levels of *IFNGR1* exhibited longer
299 progression-free survival compared to the higher expressing group (**Fig. S3I**).
300
301 **IRF1 targets mediate pro-survival and anti-proliferative programs in DTCs**
302 We next sought to examine mechanisms by which IFNγ signaling promotes metastasis.
303 *Ifngr1* knockout did not alter cancer cell fitness under standard adherent culture
304 conditions in the presence or absence of IFNγ treatment, evidenced by comparable

305 colony count formation (**Fig. 4A**). IFN-γ had similarly no impact on cancer cell survival
306 as measured by CellTiter-Glo luminescent cell viability assay under regular culture
307 conditions (**Fig. 4B**). Interestingly, IFNγ treatment had a protective effect and increased
308 cell viability in sgNTC cells under ultra-low attachment (ULA) conditions (**Fig. 4C**). This
309 protective effect was ablated in the *sgIfngr1* group (**Fig. 4C**). Moreover, we observed
310 that knockout of downstream *Stat1* and *Irf1* transcription factors (**Fig. S4A & S4B**)
311 phenocopied *Ifngr1* knockout under ULA and IFNγ treatment conditions (**Fig. 4D**). Irf1 is
312 a transcription factor downstream from Ifngr1/Stat1 signaling. As Irf1 knockout did not
313 rescue the survival phenotype (**Fig. 4D**), this suggests that (1) Irf1 activation is
314 necessary for the pro-survival phenotype and (2) the genes necessary for increased
315 survival under low attachment conditions are likely downstream of Irf1. To investigate
316 this further, we performed RNA-based gating in the scRNA-seq dataset and defined
317 *Irf1*^{high} and *Irf1*^{low} cancer cell populations (**Fig. 4D**). We created custom module scores
318 that reflected common pathways cancer cells use to resist anoikis-mediated death:
319 autophagy, stress, and pro-survival/anti-apoptosis[33] (**Fig. 4D**). Out of the three modules
320 tested, *Irf1*^{high} cells most significantly upregulated the pro-survival/anti-apoptosis module
321 (**Fig. 4F**, right panel). One of the top upregulated genes in the *Irf1*^{high} population was
322 *Stat3* (belonging to the pro-survival module) (**Fig. 4G, Fig. S4C**). The IL-6/JAK/STAT3
323 signaling axis is known to promote cancer cell survival by regulating the expression of
324 anti-apoptotic genes[34]. Indeed, anti-apoptotic Stat3 target genes, *Mcl-1* and *Bcl2*[35],
325 were significantly upregulated in *Irf1*^{high} cells (**Fig. 4H**). Socs3 is a known marker of
326 active Stat3 signaling and is responsible for dampening the JAK/STAT pathway[36]. We
327 confirmed *Socs3* upregulation in this population of cells (**Fig. S4D**). Next, we
328 experimentally tested pStat3 activation under ultra-low attachment and IFNγ treatment
329 conditions. As predicted based on the scRNA-seq modules (**Fig. 4F**), SQSTM1
330 (autophagy marker) levels were unaltered with IFNγ treatment in WT cells, while pStat3
331 increased (**Fig. 4I**).
332
333 Interestingly, we observed increased *Btg2* expression, an anti-proliferative gene, in
334 *Irf1*^{high} cells (**Fig. S4E**). As DTCs often exhibit reduced proliferation[37], we tested *Irf1*^{high}
335 cells for an anti-proliferative/dormancy module. The dormancy module was significantly

336 upregulated in *Irf1*^{high} cells (**Fig. 4J**). Consistent with this observation, AscMet exhibited
337 reduced barcode expansion (**Fig. S4F**) and reduced *Top2a* expression (**Fig. S4G**)
338 compared to OmMet. Moreover, module scoring in patient TCGA-OV dataset[32] yielded
339 moderate positive correlations of pro-survival and dormancy programs to IFNγ response
340 (**Fig. S4H**). Collectively, these results suggest that, while the loss of *Ifngr1* does not
341 affect cancer cell growth *in vitro*, under low attachment and IFN-γ-rich conditions that
342 mimic ascites environment, DTCs upregulate an Irf1/Stat3-driven pro-survival module
343 and are phenotypically less proliferative.
344
345 **Pro-inflammatory TAMs in ascites are distinct from omental TAMs**
346 Next, we considered whether ascites priming of cancer cells occurs via autocrine
347 signaling or through interactions with the metastatic niche microenvironment. To identify
348 IFNγ producers and responders within the ovarian metastatic niche, we first examined
349 the expression patterns of IFNγ and IFN-responsive genes identified in our CRISPR
350 screen. Analysis across all cells (**Fig. 5A, S5A & S5B**) revealed that the T/NK cell
351 populations are the main producers of IFNγ, while the downstream CRISPR hits
352 (*Gbp2b*, *Marco*, *Ms4a8a*, *CD300lb*, and *Slfn1*) are mainly expressed in the myeloid
353 fraction, at higher levels compared to tumor cells (**Fig. 5A**). CellChat[38] analysis
354 identified a significant increase in both the number and strength of cell-cell interactions
355 between cells from naïve and metastasis-derived samples (**Fig. S5C**). Tumor cells
356 primarily interacted with myeloid cells in both ascites in omentum (**Fig. 5B**). Additionally,
357 stromal interactions were enriched in the metastatic omentum (**Fig. 5B**). These results
358 suggest that interaction between IFNγ-responsive tumor cells and macrophages may be
359 a key axis of communication in ovarian metastasis. Focusing on the myeloid
360 compartment, we grouped Seurat clusters into broader cell identity categories (**Fig. S5A**
361 **& B**) and found a proportional increase in myeloid cells in both metastatic sites
362 compared to their naïve counterparts (**Fig. 5C**). Subclustering the myeloid population
363 revealed that the major contribution to the proportional increase are subclusters 0,1, 5,
364 and 6 (**Fig. 5D, Fig. S5D**). These macrophage subclusters were identified as tumor-
365 associated macrophages (TAMs) based on high expression of *Adgre1*, *Cd68*, *Csf1r*,
366 *Itgam*, *Mertk*, and *Trem2* (**Fig. S5E**). RNA velocity analysis revealed a dynamic

transition from the ascites-derived TAM clusters 1 and 5 toward omental TAM clusters 0 and 6 (**Fig. 5E**). Omental clusters 0 and 6 were characterized by increased expression of costimulatory molecules and interleukin 1 family genes as compared to ascites clusters 1 and 5 (**Fig. 5F, Fig. S5F**). Collectively, the RNA velocity and DEG analyses suggest that ascites-derived TAMs may represent a less differentiated or "primitive" state relative to omental TAMs.

Hybrid functional state of omental TAMs is accompanied by an increase in activated and regulatory T cells

Given the apparent macrophage niche-dependent differentiation states, we next asked whether omental TAMs reflect a polarized, terminal state within the metastatic niche. If so, increased TAM polarization would likely shape the T cell compartment[39,40]. Indeed, while the ascites-derived T/NK compartment was dominated by a mixture of naïve CD4+ and CD8 +T cells, omental metastases and niche tissue contained a broader and more complex repertoire of activated, exhausted, and regulatory T cells (**Fig. 5G**) enriched in pathways related to regulation of immune cell activation (**Fig. S5G**). We next subsetted macrophages (*Cd68*^{high}/*Adgre1*^{high}, **Fig. S5H**) and scored them against M1 and M2 gene modules. Compared to ascites-derived TAMs, omental TAMs exhibited higher hybrid functional state scores (**Fig. S5I**), reflecting an immunomodulatory TAM cellular state[41] that cannot be fully captured by binning into a strictly immune-promoting or suppressing category. Unlike the immunomodulatory and ECM-related omental signatures, ascites-derived TAMs were enriched in pathways associated with cellular stress responses and NRF2-dependent redox metabolism (**Fig. 5H & 5I**). On the gene level, ascites TAM signatures were reflected in elevated expression of key stress-related genes – including *Anxa1* and *Hmox1* – as well as *Ndufb8* and *Cox5a*, components of mitochondrial respiration (**Fig. S5J**). These findings indicate that ascites TAMs may represent an earlier, less polarized yet metabolically active state, while omental TAMs have transitioned into an immunomodulatory, polarized phenotype.

To characterize prevalent interactions between omental TAMs and T/NK cells compared to ascites, we applied NicheNetR, a computational tool used to predict receptor-ligand

interactions[42] (**Fig. S6A**). NicheNetR comparison between the two anatomical locations revealed *Cd80* interacting with *Cd28*, *Cd274* (PD-L1 transcript), and *Ctla4* as prevalent interactions between myeloid cells and T/NK cells in the metastatic omentum (**Fig. S6B**). *Cd80* was strongly expressed and upregulated in omental compared to ascites TAMs (**Fig. S6C**). Cd80 engagement with Cd28 and Ctla4 are necessary interactions for co-stimulation and co-inhibition of T cell activation, respectively[43]. Cd80 interaction with Cd274 is a less characterized interaction that can occur bidirectionally and leads to T cell inhibition, similar to the PD-1/PD-L1 signaling axis[44]. Next, we utilized flow cytometry to validate immune cell dynamics observed in the scRNA-seq dataset (**Fig. S6D-H**). GFP+ cancer cells were detected in both metastases-bearing ascites and omentum samples (**Fig. S6D**). While there was a significant increase in CD11b+/CD11c+ macrophages as well as CD11b-/CD11c+ DCs in ascites (**Fig.S6E & F**), metastatic omentum samples were significantly enriched in mature F4/80+ TAMs (**Fig. S6G**) and cytotoxic CD8+ T cells (**Fig. S6H**). These findings further implicate the omental environment in fostering a highly immunomodulatory population of TAMs.

Peritoneal macrophages protect cancer cells against anoikis-mediated cell death

Although TAM-induced immunomodulation is a well-established, significant metastasis driver, less is known about the role of direct TAM-tumor cell interactions. To identify cells that are in close contact with ovarian metastases, we developed a Cre-based iteration of the “NicheTracing” system to genetically mark and trace microenvironmental contacts *in vivo* over a prolonged timeframe. In this system, cancer cells expressing Cre.ERT2 were injected into Ai6 (RCL-zsGreen) Cre reporter mice. Upon cytoplasmic and nuclear entry of Cre into neighboring cells, Cre-mediated recombination turns on the zsGreen cassette in host cells (**Fig. 6A**). After validating Cre.ERT2 expression in transduced cell lines (**Fig. S7A**), we benchmarked this system using *in vitro* coculture (**Fig. S7B-S7F**) and in an independent model of triple-negative breast cancer (TNBC) lung metastasis established using the E0771 cell line (**Fig. S7G & S7H**). In the ovarian metastasis model, we readily detected zsGreen+ (ZsG) niche cells in both metastasis-bearing omentum and ascites at the experimental endpoint six weeks post cancer cell injection (**Fig. 6A**). We performed flow cytometry analysis on ascites and gated cells into ZsG^{low}

429 and ZsG^{high} (**Fig. 6B**, top panel). Unlike ZsG cells detected in lung metastases (**Fig.**
430 **S7H**, right panel), over 90% of ZsG^{high} host cells were F4/80^{+}/Ly6G^{low} TAMs (**Fig. 6B,**
431 bottom panel, **Fig. 6D**).
432
433 We next asked if peritoneal TAMs actively promote ovarian cancer metastasis.
434 Macrophage depletion via direct i.p. liposomal chlodronate injections (**Fig. 6E**)
435 demonstrated that peritoneal TAMs are pro-metastatic: depleting TAMs significantly
436 reduced omentum weights (**Fig. 6F, Fig. S7I**) and CD45 negative cancer cell
437 frequencies in ascites at experimental endpoint (**Fig. 6G, Fig. S8A** flow gating strategy).
438 We next explored whether macrophages could promote cancer cell survival under low
439 attachment conditions, akin to the effects observed with IFNγ treatment (**Fig. 4F**). To
440 test this, we performed a macrophage-cancer cell coculture under ultra-low attachment
441 (ULA) conditions. Macrophages from peritoneal lavage were enriched using F4/80
442 magnetic beads (**Fig. 6H**, **Fig. S8B & S8C** flow gating strategy) and cocultured with
443 three different murine ovarian cancer cell lines; ID8 p53$^{-/-}$, ID8 p53$^{-/-}$ BRCA2$^{-/-}$, and
444 PPNM[45] (**Fig. 6I-K, S8D** flow gating strategy). After a 48-hour coculture period, flow
445 cytometry analysis revealed that cancer cell viability, as measured by live/dead staining
446 (ZombieAqua), decreased under ULA conditions compared to regular attachment
447 plates. Most importantly, survival was partially rescued with macrophage coculture
448 across all three cell lines (**Fig. 6I-K**). These results indicate that peritoneal macrophages
449 directly support cancer cell survival under conditions mimicking the low attachment,
450 ascites environment.
451
452 **Patient ascites-derived TAM-Tumor interactions are enriched in pro-survival**
453 **pathways**
454 To determine if tumor-supportive macrophage interactions occur in human ovarian
455 cancer, we analyzed a human-derived single-cell dataset containing over 200,000 single
456 cells from 14 ovarian cancer patients and collected from five locations: peripheral blood
457 (PB), peripheral lymph nodes (PLN), malignant ascites (Asc), primary tumor (Pri.OT),
458 and matched metastatic tumor (Met.Ome)[46]. As observed in our murine dataset, cancer
459 cell-containing compartments, including Asc/Pri.OT/Met.Ome, had increased

460 proportions of macrophages compared to PB and PLN (**Fig. 7A, S9A & S9B**). DEG
461 analysis between TAMs at metastatic sites (Fig. 7B) and subsequent GO pathway
462 analysis conducted on the DEG list revealed immune-modulatory pathways (cytokine,
463 chemokine, allograft rejection), EMT, TNFα, and KRAS signaling upregulated in
464 Met.Ome TAMs (**Fig. 7D, S9D**). In Asc TAMs, the pathways were predominantly
465 metabolism and cargo receptor activity related (**Fig. 7E, S9E**).
466
467 We applied NicheNetR analysis to further characterize TAM-to-tumor cell interactions in
468 ascites. We implemented this strategy to both our murine dataset as well as the patient
469 dataset (**Fig. 7F**). After defining myeloid cells (Broad cell ID) as the sender cell type in
470 the murine dataset and macrophage cluster as the sender in the human dataset, we
471 compared the top predicted tumor-interacting ligands in each dataset. We found 4
472 overlapping sender ligands across species (**Fig. 7F**) - *TGFB1*, *IL10*, *TNF, and IL1B* -
473 that were the most significant ligands predicted to interact with cancer cell receptors
474 (**Fig. 7G**). Next, we examined the top predicted downstream target genes in cancer
475 cells affected by top TAM ligands (**Fig. S9F**). ORA pathway analysis of the predicted
476 downstream genes yielded several pathways involved in cell-cell adhesion, response to
477 oxygen levels, and other tumor-promoting pathways (**Fig. 7I**). Together, these data
478 suggest that patient-derived Asc TAMs may function similarly to murine TAMs in directly
479 supporting ascites cancer cells.
480
481 **DISCUSSION**
482
483 **Early DTC dominance phenotype in ovarian cancer metastasis**
484 DTC-niche interactions at each stage of the metastatic cascade fundamentally
485 determine disease progression and patient outcomes. Following the initial wave of
486 metastatic dissemination, early DTCs inevitably reshape the metastatic niche
487 microenvironment, irrespective of whether they ultimately survive or perish upon arrival.
488 The niche remodeling by pioneer DTCs likely exerts more profound effects on
489 subsequent colonization than distant signals from the primary tumor. While the pre-
490 metastatic niche (PMN) has been extensively characterized[47,48] , this dynamic process

following DTC seeding creates what we term the Post-Seeding Metastatic Niche (PSMN). The multi-cellular dynamics resulting from progressive DTC accumulation at newly colonized PSMN mirrors a well-established ecological concept: the Allee effect, which describes how population growth rates depend on population density through competition or cooperation. Although the Allee effect has been demonstrated in metastatic contexts using in vitro models[49], how continuously arriving DTCs dynamically alter PSMN properties and influence the fate of later-arriving tumor cells within the intact physiology of living systems remains unstudied.

Leveraging our MetTag barcoding and staggered injection model, the data presented here consistently demonstrated a skewed overrepresentation of early disseminated tumor cells (DTCs): TP-1 and TP-2 DTCs overwhelmingly dominate the metastatic burden at day 40, whereas cells introduced at later days (TP-6) showed minimal contributions to final overt metastases. This pattern persists across immunocompetent, immunodeficient (NRG), and macrophage-depleted hosts (**Fig. 1**). This skewness in early DTC dominance cannot simply be attributed to inherent, longer chronological growth times of early DTCs, as there remains an ample growth window for TP-6 cells (from Day 11 to Day 40). We put forward several non-mutually exclusive hypotheses that could explain early DTC dominance in our study. First, the omentum might contain a limited number of permissive micro-niches that favor DTC colonization. Pioneer DTCs might rapidly saturate these micro-niches and monopolize spatial resources – a “first come, first served” model. Second, the immune-independent nature of skewed distribution of temporally disseminated DTCs suggests a role of non-immune stromal elements in dictating colonization success. Early DTCs may actively remodel the niche, rendering it unfavorable for later DTCs. Comprehensive spatiotemporally resolved imaging and genomics analyses are required to further explore these hypotheses.

Duality of IFNγ signaling-driven metastatic adaptation

Beyond the “seed and soil” hypothesis, it has been increasingly appreciated that metastasis is not merely passive fitness-based selection of DTC clones at the niche, but also an active epigenetic DTC-niche mutual adaptation process. Our single-cell

522 transcriptome analysis, coupled with barcoding clonal analysis, provided us with clonal
523 resolution of the underlying genetic and epigenetic determinants governing DTC
524 behavior. Interestingly, instead of occupying unique transcriptome clusters - which
525 would likely suggest distinctive genetic mutational features - the expanded clones form
526 similar coordinated adaptive “mini-ecosystems” encompassing multifaceted
527 transcriptome features that converge toward an inflammatory/IFNγ response (**Fig. 2H-**
528 **L**). Our CRISPR/Cas9 *in vivo* screen results (**Fig. 3**) further supported the notion that
529 cancer cell fitness in the peritoneal cavity and subsequent omentum metastasis
530 depends on rapid transcriptional-level adaptation to activate IFNγ-responsive programs
531 in ascites. Our findings extend the conventional view of genetically pre-determined
532 clonal fitness in the metastatic cascade. In this “first come, first served” model, early
533 metastatic niche sensing and epigenetic adaptation in the race towards occupying
534 permissive micro-niches ultimately determines metastasis success.
535
536 Although the findings presented here support a tumor cell-centric pro-metastatic role of
537 IFNγ, it is important to note that IFNγ in metastatic niches can act in complex ways. In
538 some cancers, IFNγ reduces metastasis through activation of effector T and NK cells,
539 thereby enhancing the effectiveness of immunotherapy[50,51]. Furthermore, in some
540 contexts, IFNγ can induce apoptosis in regulatory T cells and inhibit angiogenesis[52].
541 Specifically in ovarian cancer cells, both anti-metastatic and pro-metastatic roles have
542 been reported[53,54]. For the latter, IFNγ has been previously reported to upregulate PD-
543 L1 and IL-8 in ovarian cancer cells, leading to increased cell migration and
544 proliferation[54]. We did not observe any proliferation differences via colony formation
545 assay *in vitro* (**Fig. S4F**) after a 7-day IFNγ exposure, and our scRNA-seq data suggest
546 that IFNγ programs are associated with dormancy *in vivo* (**Fig. 4J & S4**). Based on the
547 data presented here, we believe that, although both effector immune cells and cancer
548 cells could be impacted by IFNγ, IFNγ response by cancer cells (intrinsically) leads to an
549 overall pro-metastatic effect that outweighs the anti-metastatic roles in ovarian cancer.
550 In particular, although both ascites and omental TAMs in our study closely resembled a
551 *Trem2*/*Apoe*-high state described elsewhere[55], we found that they exhibited niche-
552 specific adaptations promoting divergent functions (**Fig. 5**).

553

554 In summary, our study dissected the complex landscape of ovarian cancer metastasis
555 through a systematic characterization of both cancer cells and local immune factors
556 using MetTag temporal, clonal and scRNA-seq analysis. Our findings highlight the
557 importance of ascites as a functional reservoir for these factors and the early acquisition
558 of IFNγ response as a necessary adaptation step for DTCs to survive and colonize at
559 the omentum.

560

561 **ACKNOWLEDGMENTS**

562 This study was partially funded by the NIH T32GM075762 training grant (E. A.), NIH
563 R01 CA194697-01(S.Z.), NIH R01 CA255064-01A1(S.Z.), NIH R21 CA263798-01
564 (S.Z.), and the Cancer Prevention and Research Institute of Texas (CPRIT) Scholar
565 Award RR220024 (S.Z.). We are additionally grateful to the Dee Family endowment
566 (S.Z.) and to the following core facilities: Notre Dame Freimann Life Sciences Center,
567 Notre Dame Genomics and Bioinformatics Core Facility, Indiana University School of
568 Medicine Center for Medical Genomics, Indiana University Simon Cancer Center,
569 Simmons Comprehensive Cancer Center, UT Southwestern (UTSW) Animal Resource
570 Center, UTSW Flow Cytometry Core, and UTSW Small Animal Imaging Core Facility.
571 The computational arm of this research project was, in part, supported by the BioHPC
572 supercomputing facility at UTSW.

573

574 **AUTHOR CONTRIBUTIONS**

575 Conceptualization and experiment design, E.A., M.S.S. and S.Z.; Data analysis, E.A.,
576 S.Z., X.L., Z.Z.; Experiments and methodology, E.A., S.Z., S.R.F., S.M.G., J.L., W.M.,
577 N.D., T.C.R., M.Z.; Manuscript writing and revision, E.A., S.M.G., and S.Z.; Study
578 supervision, S.Z. We attest that all coauthors reviewed and pre-approved the
579 manuscript before submission.

580

581 **DECLARATION OF INTERESTS**

582 We do not have any competing interests to declare.

583

584

585 **FIGURE LEGENDS**

586

587 **Figure 1: Tracking Clonal Lineage in Ovarian Cancer Metastasis**

588

589 (**A**) Schematic depicting main elements of the MetTag library barcoding construct. (**B**)
590 Schematic of injection and tissue collection timeline for the staggered injection
591 experimental model using MetTag-barcoded ID8 $p53^{-/-}$ ovarian cell lines. Schematic was
592 partially created with BioRender.com. (**C**) Genomic DNA (gDNA)-level barcode
593 distributions in the omentum graphed as frequency under WT, NRG, and MAC depletion
594 conditions. (**D-E**) gDNA-level barcode distributions in ascites and pelvic fat pads under
595 WT and NRG conditions. In (C-E) panels, BC.ID1 = TP-1, BC.ID2 = TP-2, BC.ID3 = TP-
596 3, BC.ID4 = TP-4, BC.ID5 = TP-5, BC.ID6 = TP-6 for clarity. (**F**) Injection schema for
597 comparing one-time (400,000 total, n = 10) cell dose and fractionated (2,400,000 total, n
598 = 10) cell injections (left) and representative BLI images at endpoint (right). (**G**) Bar
599 graph depicting total flux emission in each group at experimental endpoint. (**H**)
600 Schematic of scRNA-seq experiment conducted using a reversed BC.ID injection order.
601 LARRY barcodes are readily captured by Chromium 10x Feature Barcoding. (**I**) Pie
602 charts of RNA-level barcode frequencies in each location grouped as early (BC.ID5,
603 BC.ID6), mid (BC.ID4, BC.ID3), and late (BC.ID2, BC.ID1). (**J**) Heatmap of sample level
604 barcode frequencies, BC.ID6 = TP-1, BC.ID5 = TP-2, BC.ID4 = TP-3, BC.ID3 = TP-4,
605 BC.ID2 = TP-5, BC.ID1 = TP-6. (**K**) Volcano plot of DEGs between early and late
606 timepoint barcoded cancer cells where threshold for significance was defined at $p < 0.05$
607 and $log2FC < -1.0$ for downregulation or >1.0 for upregulation. Genes labeled are the
608 top 30 genes based on significance. Data in Figure 1G was analyzed using a two-tailed
609 Student's t test and graphed as mean with standard deviation (SD). In Figure 1K, the
610 DEG table was generated using the Seurat FindMarkers() function and p values
611 calculated via a Wilcoxon rank-sum test. For all Wilcoxon rank-sum tests, p values
612 graphed represent the adjusted p value.

613

614 **Figure 2: Clonal Analysis Reveals Shared Evolutionary Path Towards**
615 **Inflammatory Signature**
616
617 (**A**) Split UMAP depicting cluster distributions across the four experimental conditions
618 and identifying cancer cell-enriched clusters in ascites and omentum. (**B**) Reclustered
619 cancer cell UMAP colored by the two metastasis-bearing anatomical locations. (**C**)
620 Stacked bar chart depicting the frequency of Seurat subclusters within each metastatic
621 location. (**D**) Seurat cluster UMAP of reclustered cancer cells with transcriptional
622 program labels. (**E**) Dot plot depicting Hallmark pathways across all subclusters used to
623 define each cluster subset gene program in (D). (**F**) Schematic representation of the
624 possible outcomes of LARRY clonal analysis based on transcriptome patterns of
625 enriched clones. (**G**) Heatmap of normalized clonal LARRY barcode counts across the
626 two anatomical locations and individual mice (HTOs). (**H**) UMAP overlay of top 3
627 expanded clones in the omentum. (**I**) Bar chart depicting the relative subcluster
628 proportions present in each of the top 3 barcode clones. (**J**) scVelo-generated PAGA
629 velocity graph indicating trajectory arrows and inferred cluster lineage. (**K**) scVelo and
630 CellRank-based simulated path from start to endpoint clusters. (**L**) Violin plot depicting
631 RNA-level contribution of each timepoint to the IFNγ signature. Data in Figure 2L was
632 analyzed by first defining the IFNγ signature using canonical mouse genes, followed by
633 directly applying the wilcox.test() function in Seurat to compare TP-1 and TP-6
634 expression.
635
636 **Figure 3: Activation of IFNγ Response in Ascites is Necessary for Successful**
637 **Omental Colonization**
638
639 (**A**) DEG-based volcano plot of gene expression differences between OmMet and
640 AscMet, where threshold for significance was defined at $p < 0.05$ and $\log2FC < -1.0$ for
641 downregulation or >1.0 for upregulation. (**B**) Boxplots comparing IFN signature modules
642 between AscMet and OmMet. (**C**) Schematic describing *in vivo* ovarian metastatic niche
643 signature screen. Partially created with BioRender.com. (**D**) *In vivo* CRISPR screen
644 RankView plots generated using MAGeCKFlute. OmMet (n=5) and AscMet (n=4)

645 samples were compared to the original pool of ID8 p53$^{-/-}$ cells. (**E**) Ranks of individual
646 sgRNAs targeting positive control *Pten* and depleted genes. (**F**) Lollipop plot of depleted
647 pathways associated with depleted genes in Fig. 3E. (**G**) IFNγ treatment time course
648 qPCR plots of select CRISPR hits and positive controls. (**H**) IFNγ treatment time course
649 western blot probing for Stat1/pStat1 and GBP1. (**I**) Schematic of *in vivo* experimental
650 metastasis study comparing sgNTC and sgIFNGR1.g1 groups. (**J**) Time course log10-
651 transformed total emission/flux values (left). Two independent groups pooled; cohort 1
652 NTC n = 8, KO n = 7; cohort 2 NTC n = 5, KO n = 5. log10-transformed flux plot for
653 week six with p value (right). (**K**) Kaplan Meier survival curve generated for cohort 1.
654 Data in Figure 3B was analyzed by first defining IFN signatures, followed by applying
655 wilcox.test() in Seurat to compare AscMet and OmMet. CRISPR screen related data
656 (3D-F) was first analyzed using MAGeCK. Count summary, gRNA summary, and gene
657 summary output files were loaded into RStudio to generate rankview plots using
658 MAGeCKFlute. For Figure 3G, qPCR data was analyzed by averaging technical
659 replicates for each biological replicate, followed by calculating dCq by normalizing target
660 gene Cq to housekeeping gene control. Next, 2^(-ddCq) or fold change was calculated
661 by normalizing the values to the zero hour (PBS) treatment samples and plotted in
662 Prism GraphPad. Significance between groups was assessed using a two-tailed
663 Student's t test and data was plotted as mean with standard deviation (SD). Data in
664 figure 3J left panel was plotted as log transformed mean with 95% confidence interval
665 (CI) and a two-tailed Student's t test was performed at each timepoint. Data in 3J right
666 panel was plotted with median log transformed values.
667
668
669 **Figure 4: IFN-γ Sensing Mediates Resistance to Anoikis and Activates Pro-**
670 **survival Signaling**
671
672 (**A**) Colony formation assay performed without (left) or with (right) 100 ng/ml IFNγ. (**B-C**)
673 Cell-Titer Glo assay luminescence CTG values graphed as fold change for regular
674 culture conditions (B) and ultra-low attachment conditions (C), with and without IFNγ
675 treatment. Fold change was determined by normalizing each cell line's CTG value to the

676 regular attachment, no IFNγ treatment condition. (**D**) CTG flux value dot plots for Stat1-
677 KO and Irf1-KO cells under ultra-low attachment, with or without IFN-γ treatment. (**E**)
678 scRNA-seq based gating strategy used to identify Irf1-high and low cells for module
679 scoring. (**F**) Violin plots for autophagy, stress, and pro-survival (anti-apoptotic) scores in
680 Irf1-high vs. Irf1-low cells. Violin plots comparing Stat3 (**G**), Mcl-1, and Bcl2 (**H**)
681 transcript levels between Irf1-high, mid, and low cells. (**I**) Western blot probing for Stat3
682 activation and SQSTM1 expression under ultra-low attachment conditions, with or
683 without IFNγ treatments. (**J**) Violin plot of dormancy module comparing Irf1-high and low
684 cells. CTG assay luminescence data (4B-4D) was analyzed in Prism using student's t
685 test. Data in B and C was graphed as mean and standard deviation, data in D was
686 graphed as median values. Anoikis and dormancy modules, along with Stat3, Mcl-1,
687 and Bcl2 transcript expression levels were compared between Irf1-high and Irf1-low
688 cells by applying the wilcox.test() function in Seurat.
689
690
691 **Figure 5: Ascites and Omental TAMs Differ in Their Immunomodulatory Potential**
692
693 (**A**) Violin plots depicting CRISPR screen hits expression level across Broad cell ID
694 categories (cell types). (**B**) CellChat-generated circus plots of interaction strengths
695 between Broad cell ID categories in metastatic omenta (left) and ascites (right). (**C**)
696 Stacked bar chart of cell type proportions across the four experimental groups. (**D**)
697 UMAPs of reclustered myeloid cells, split by experimental condition. (**E**) scVelo RNA
698 velocity plot showing arrows pointing from ascites TAMs (clusters 1 and 5) to omentum
699 TAMs (clusters 0 and 6). (**F**) DEG volcano plot comparing gene expression differences
700 between ascites TAM cluster 1 and omentum TAM cluster 0. (**G**) Stacked bar chart of
701 subsetted T/NK cells comparing cell proportions in ascites and omentum. (**H-I**) ORA
702 generated Reactome pathways enriched in ascites (left) and omentum-derived TAMs
703 (right). Significance of DEGs in Figure 5F was evaluated by applying the FindMarkers()
704 and Wilcoxon test in Seurat to compare ascites and omental *Cd68*^{high}/*Adgre1*^{high}
705 macrophages.

706

707

708 **Figure 6: NicheTracing Identifies Ascites-derived TAMs as Pro-Metastatic**
709 **Interactors**

710

711 (**A**) Schematic describing the Cre-based NicheTracing labeling system where ID8 p53$^{-/-}$
712 and E0771 cancer cells express Cre.ERT2 which transfers to neighboring RCL-ZsGreen
713 niche cells. Upon nuclear entry of Cre.ERT2, labeled niche cells turn ZsGreen positive
714 (ZsG+). (**B**) Representative gating strategy depicting the major cell population tagged
715 with zsG. (**C-D**) Bar plots showing preference for F4/80+ macrophage labeling in
716 ascites. (**E**) Liposomal chlodronate-based macrophage depletion strategy and timeline
717 schematic with representative tissue images. n= 7 liposome control group and n = 7
718 chlodrosome treatment group. (**F**) Bar plot showing quantification of omental
719 metastases via omental weight measurement at endpoint. (**G**) Images of ascites
720 samples harvested at endpoint for flow cytometry analysis (left) and flow-based
721 quantification of CD45 negative cells (right). (**H**) Schematic of macrophage-cancer cell
722 coculture layout (top) and representative coculture images for one cell line (bottom). (**I-**
723 **K**) Plots of percent CD45 negative cancer cell viability post coculture. Data in Figures
724 6C-D and 6F-6H was plotted as mean with SD and differences between groups were
725 compared via a two-tailed unpaired Student's t test. Data in Figures 6I-K was similarly
726 analyzed using a Student's t test and plotted with median values.

727

728

729 **Figure 7: Patient Ascites MAC/Tumor Interactions are Enriched for Tumor-**
730 **supporting Pathways**

731

732 (**A**) Stacked bar chart of main cell type proportions captured in human scRNA-seq
733 dataset across five anatomical locations, using maintype-2 annotation provided by
734 publisher. (**B**) Heatmap depicting DEGs between Met.Ome and Ascites. (**C-D**) GO
735 Molecular Function pathway level differences between omental MACs (C) and ascites
736 MACs (D). (**E**) Schematic depicting NicheNetR analysis approach for finding top TAM

ligands in both murine and human datasets. This panel was partially generated using BioRender.com. (**F**) Venn diagram of top NicheNet predicted ligands after filtering for robust expression and overlapping with top interactions in our murine dataset. (**G**) Heatmap showing top receptor-ligand interactions upregulated in patient ascites-MACs compared to metastases. (**H**) GO enrichment dotplot generated from the gene list containing top target genes in cancer cells that are predicted to respond to top ligands in the human dataset. Data in Figure 7B was analyzed using the FindMarkers() function in Seurat and Wilcoxon test to compare Asc and Met.Ome.

SUPPLEMENTAL INFORMATION (Including Supplemental Figures S1-S9)

Figure S1. MetTag Tracing Construct and Metastatic Model Validation

(**A**) Schematic depicting MetTag library barcoding plasmid, and modes of detection upon plasmid integration: DNA level, Pol III U6 driven RNA level, and Pol II CROP-seq based. (**B-C**) Barcode frequencies comparing relative eaviness of library distribution across BC.ID batches (B) and original depositor LARRY library (C). (**D**) Table depicting unique reads detected in each library batch after MiSeq sequencing and read filtering. (E-F) Representative ascites images and dissecting scope images of GFP+ metastases formed under the repeated injection schema. (F) Bar chart depicting macrophage depletion in chlodrosome treatment group at experimental endpoint (right). (**G**) Representative gating strategy (left) and quantification of GFP+ tumor cells in ascites under macrophage depletion conditions (right). Data in Figures S1F and S1G was plotted as mean with SD and differences between groups were compared via a two-tailed unpaired Student's t test.

Figure S2. scRNA-seq-based Tumor Cell Identification and Cancer Cell Velocity

765 (**A**) Feature plot of main marker genes used to define and subset cancer cells. (**B**)
766 Heatmap of reclustered cancer cell marker genes. (**C**) Violin plots of top defining cluster
767 marker genes. (**D**) Escape generated Hallmark pathways each represented by a
768 different color. (**E**) Escape pathway-based violin plots of each pathway class in (D). (**F**)
769 UMAPs depicting main pathway signatures represented in the top three clonally
770 expanded barcoded cells. (**G**) CellRank-generated initial and terminal cellular states
771 overlayed on the cancer cell UMAP. (**H**). Violin plot of IFNα signature score across the
772 six different BC.ID timepoints. Data in Figure S2H was analyzed by first defining the
773 IFNα signature using Hallmark IFNα response genes, followed by directly applying the
774 wilcox.test() function in Seurat to compare TP-1 and TP-6 signature expression.

775

776 **Figure S3. *In vivo* CRISPR Screening and IFN Signaling in AscMet and OmMet**

777 (**A**) ORA-generated Hallmark pathways based on DEGs between AscMet and OmMet.
778 (**B**) Heatmap depicting IFN response gene scoring differences between AscMet and
779 OmMet. (**C**) Western blot validation of SpCas9 expression in ID8 p53$^{-/-}$ cells after
780 PiggyBac transposon transfection and selection with hygromycin. (**D**) Representative
781 flow cytometry generated histogram of mCherry fluorescence (left) and bar chart
782 depicting percent mCherry positive cells five days after lenti-guide transduction (right).
783 (**E**) Violin plot of *Ifngr1* expression levels in cancer cells *in vivo*. (**F**) Representative flow
784 cytometry generated histogram of IFNGR1 surface expression in knockout vs. wild type
785 cells (left) and bar chart with quantification of IFNGR1 mean fluorescent signal changes
786 (right). (**G**). Western blot probing for IFNγ downstream transcriptional targets, Stat1 and
787 Gbp2b in *Ifingr1* knockout cells. (**H**) Endpoint (week six) BLI images of sgIFNGR1
788 compared to sgNTC experiment cohort 1 mice. (**I**) KMPlotter-generated Kaplan Meier
789 progression free survival curve comparing low and high IFNGR1 expression at stage III
790 and stage IV. IFNα/IFNγ signatures in Fig. S3B were described in previous figures. Data
791 in (D) and (F) was analyzed in GraphPad Prism using a two-tailed Student's t-test and
792 graphed as mean with SD. Fig. S3E violin plot Ifngr1 expression levels were compared
793 using the wilcox.test() function in Seurat.

794

795 **Figure S4. IFNγ-induced Pro-Survival and Dormancy Programs**

796 (**A-B**) Western blots showing protein levels of Stat1, Irf1, and Gbp2b under Stat1 (A) or
797 Irf1 (B) knockout, with IFNγ treatment. (**C**) Volcano plot of DEGs between Irf1-high and
798 Irf1-low cancer cells. (**D-E**) Violin plots showing Stat3-related *Socs3* and *Btg2* transcript
799 expression level differences between Irf1-high, mid, and low cancer cells. (**F**) Stacked
800 bar plot binning AscMet and OmMet cancer cells into frequency categories based on
801 LARRY barcode expansion score: freq. 1 = no clonal expansion, freq. 2-5 = moderate
802 clonal expansion, and freq. 5+ = high clonal expansion. (**G**) Violin plot comparing Top2a
803 expression levels between AscMet and OmMet. (**H**) Correlation plots generated from
804 the TCGA-OV dataset; top panel represents the correlation between pro-survival and
805 IFNγ modules, bottom panel represents the correlation between dormancy and IFNγ
806 modules. DEG analysis in (C) was performed using the FindMarkers() function in
807 Seurat. p-values in (D-E) and (G) were obtained from a wilcox.test(). For Fig. S4H,
808 Pearson correlation coefficients and p-values were obtained after ssGSEA scoring. The
809 correlation curves are plotted with a linear regression line with shaded 95% CI intervals.

810

811 **Figure S5. Ascites and Omentum Immune Cell Characterization**

812 (**A**) UMAP depicting all cells captured across four sequenced groups. (**B**)
813 "Broad_cell.ID" classification of Seurat clusters into cell types based on cluster marker
814 genes. (**C**) CellChat generated bar charts depicting number of interactions (left) and
815 interaction strength (right) across the four sample groups. (**D**) Heatmap of myeloid TAM
816 subclusters 1, 0, 5, and 6. (**E**) Violin plots showing gene expression of canonical TAM
817 markers across myeloid subclusters. (**F**) Volcano plot of DEGs between myeloid cluster
818 5 and 6. (**G**) Dotplot of GO Biological Process pathways upregulated in omentum-
819 derived T/NK cells based on the DEG list comparing to ascites-derived T/NK cells. (**H**)
820 RNA-based gating strategy to subset out macrophages for subsequent analysis. (I)
821 Biaxial scatter plot of M1 and M2 module scores with overlapped ascites and omental
822 TAMs. (J) Violin plots comparing individual genes belonging to cellular response to

823 stress (Anxa1, Hmox1) and cellular respiration (Ndufb8, Cox5a) pathways between
824 omental and ascites TAMs. In (F), DEG analysis was performed using the FindMarkers()
825 function in Seurat and significance determined via Wilcoxon test. Fig. S4I hybrid score
826 and S4J violin plot expression levels were compared using the wilcox.test() function in
827 Seurat.

828

829 **Figure S6. NicheNetR Receptor-Ligand Interaction and Immunotyping Analyses**

830 (**A**) Schematic depicting cell types of interest for NicheNetR comparison between
831 omentum and ascites: receptors on T/NK cells and ligands secreted by myeloid cells.
832 (**B**) NicheNetR-generated heatmap of predicted receptor-ligand interactions. (**C**) Violin
833 plot comparing *Cd80* co-stimulatory molecule expression differences between
834 metastasis bearing omenta and ascites. (**D-H**) Flow cytometry analysis plots of cancer
835 cell and immune cell frequencies in naïve and metastatic settings: (**D**) Frequency of
836 GFP+ cancer cells, (**E**) Frequency of CD11b+/CD11c+ double positive myeloids, (**F**)
837 Frequency of CD11b-/CD11c+ dendritic cells, (**G**) Frequency of CD11b+/F4/80+
838 macrophages, and (**H**) Frequency of CD8+ T cells. S6C violin plot *Cd80* expression
839 levels were compared using the wilcox.test() function in Seurat. Flow cytometry data in
840 (D-H) was analyzed via two-tailed unpaired Student's t test and plotted with median
841 values.

842

843 **Figure S7. NicheTracing In Vitro/In Vivo Validation and Macrophage Depletion**

844 (**A**) Western blot validation of Cre expression in target cell lines: E0771 murine TNBC
845 line and ID8 p53$^{-/-}$ ovarian cancer cell line. (**B**) Schematic depicting Cre reporter used to
846 transfect HEK293T cells and Cre constructs expressed by target cells used for *in vitro*
847 assays. (**C-F**) Images generated after 72 hours of coculture with or without 2 uM 4-OHT
848 treatment. (**G**) Representative dissecting microscope images of negative control spleen
849 and lugs collected 2 weeks post E0771 retro-orbital injection. (**H**) Flow cytometry bar
850 plots at experimental endpoint showing percent switched immune cells (ZsG+) with or
851 without tamoxifen treatment (left) and within the tamoxifen treated group, frequency of

852 ZsG+ macrophages compared to ZsG- (right). (**I**) Metastasis-bearing omentum images
853 at experimental endpoint of chlodrosome-based macrophage depleted experiment. Flow
854 cytometry data in (H) was analyzed using a two-tailed unpaired Student's t test and
855 plotted as mean with SD.

856

857 **Figure S8. Flow Cytometry Gating Strategies, Related to Main Figure 6**

858 (**A**) Flow gating strategy for macrophage depletion study (left) and representative gates
859 for F4/80 macrophages in FMO, liposome control, and chlodrosome treated groups
860 (right). (**B**) Flow gating strategy for assessing MHC-II+/CD11b+ macrophage enrichment
861 following F4/80 magnetic bead isolation from peritoneal cavity. (**C**) Bar plot showing
862 relative enrichment of macrophage populations before the start of coculture. (**D**) Flow
863 gating strategy to assess CD45- cancer cell viability (Zombie Aqua negative
864 populations) after co-culture completion.

865

866 **Figure S9. Ovarian Cancer Patient Macrophage and NicheNet Analysis**

867 (**A**) UMAP depicting all (>200,000) single cells collected from five locations and
868 annotated by cell type ("Maintypes-2"). (**B**) Split UMAP of subsetted macrophage
869 clusters, split by anatomical location. (**C**) Bubble plot showing expression of top
870 NicheNet-predicted ligands in each cell type. (**D-E**) Dot plots depicting top Hallmark
871 pathways expressed in patient omental TAMs (D) and ascites TAMs (E). (**F**) NicheNet
872 heatmap depicting top ligands based on regulatory potential and downstream genes
873 affected by corresponding ligands.

874

875

876 **METHODS**

877 ***Experimental Models***

878 **Mice**

879 All animal experiments were conducted according to IACUC protocols which were pre-
880 approved by the University of Notre Dame and UT Southwestern Medical Center IACUC
881 committees. Mice were housed with unlimited access to food and water in a
882 temperature-controlled holding room with a standard 12-hour light/dark cycle. Health
883 checks were performed daily during *in vivo* experiments. Wild type C57BL/6J (B6) mice
884 were 8-10 weeks old at the experiment onset. Control and treated transgenic mice were
885 age-matched, greater than 8 weeks of age. All experiments were carried out exclusively
886 on female mice.
887 C57BL/6J (B6, 000664), NOD.Cg-*Rag1*^{tm1Mom}*Il2rg*^{tm1Wjl}/SzJ (NRG, 007799), B6.Cg-
888 *Gt(ROSA)*$^{26Sortm6(CAG\text{-}ZsGreen1)Hze}$/J (Ai6, 007906), and B6J.129(Cg)-
889 *Gt(ROSA)26Sor*$^{tm1.1(CAG\text{-}cas9*,\text{-}EGFP)Fezh}$/J (Cas9 026179) mice were obtained from
890 Jackson Laboratory (Ben Harbor, ME).
891
892 **Cell Lines**
893 The TNBC E0771 cell line (CH3 Biosystems, Amherst, NY; Cat.No. 940001-Vial) was
894 maintained in RPMI-1640 media supplemented with 10%FBS and 1%
895 Penicilin/Streptomycin (Pen/Strep). ID8 p53$^{-/-}$, ID8 p53$^{-/-}$ BRCA2$^{-/-}$, and PPNM ovarian
896 cancer cell lines, provided by the Stack lab at the University of Notre Dame, were
897 maintained in DMEM low glucose media with 5% FBS, 1% Pen/Strep, and 1% Insulin-
898 Transferrin-Selenium (ITS). PPNM cell media was additionally supplemented with 100
899 ng/ml Cholera toxin and 2ng/mL epidermal growth factor (EGF). HEK293T cells were
900 cultured in DMEM high glucose supplemented with 10% FBS, 1% Pen/Strep, and 1%
901 GlutaMAX (Gibco, 35050061). Cell cultures were grown at 37 ºC, 5% CO_2, and 95%
902 humidity. All cell lines were tested and were negative for mycoplasma contamination
903 using a routine mycoplasma PCR kit (ABM).
904
905 **Establishment and Monitoring of Experimental Ovarian Metastasis**
906 For the single-injection OvCa model, 4x10^5 ID8-LARRY.GFP or ID8-Luciferase were
907 injected into the peritoneal cavity. To ensure adequate library coverage, 2.4x10^6 ID8-
908 Cas9.Lib tagged cells were injected for CRISPR screening experiments (>1000x
909 coverage). In the repeated injection model, mice received 4x10^5 cells per injection,

910 administered six times over the course of 12 days. Mice were typically sacrificed 6
911 weeks after initial dose of cancer cells. For monitoring metastasis in luciferase-
912 expressing models, 100 ul of D-luciferin (15 mg/mL stock, GoldBio cat#: LUCK-500)
913 was administered intraperitoneally and imaged using an AMI-HTX spectral imaging
914 instrument. The total emission (flux) data for each region of interest (ROI) was obtained
915 after image analysis using the Aura software.
916
917 **Macrophage Depletion**
918 Macrophage depletion was achieved using encapsulated liposomal chlodronate
919 (Encapsula Nano Sciences, SKU# CLD-8901). Mice received a pre-treatmeant with 200
920 ul chlodrosome or empty liposome nanoparticles i.p. 24 hours before cancer cell
921 injection. Following pre-treatment, 100 ul of chlodrosome was administered twice
922 weekly throughout the study duration.
923
924 **Individual Gene Knockout Guide Cloning**
925 The CROP-seq-V2 plasmid (Addgene # 127458) was first modified to include a P2A-
926 mCherry sequence downstream of the puromycin resistance gene (PuroR) through a
927 NEBuilder HiFi DNA Assembly (NEB, E5520S) reaction. Then, single-guide RNA
928 (sgRNA) sequences were designed using CRISPick (Mouse GRCm38 reference
929 genome), oligos synthesized by IDT with BsmBI overhangs, annealed, and cloned into
930 the modified CROP-seq-V2 plasmid using the NEBridge Golden Gate Assembly Kit
931 (NEB, E1602S). The resulting plasmids were first transformed into competent *E. coli*,
932 plated on LB-ampicilin (AMP) plates, and grown at 30 ºC, before plasmid extraction.
933 Below are the sgRNA sequences used for gene targeting, including the necessary
934 BsmBI overhangs:
935 sgNTC-1 Top oligo
936 5'- **CAC CG**A CCT GAT ACG TCG TCG CGT A -3'
937 sgNTC-1 Bottom oligo
938 5'- **AAA C**TA CGC GAC GAC GTA TCA GGT **C** -3'
939 sgNTC-2 Top oligo
940 5'- **CAC CG**G TAT TAC TGA TAT TGG TGG G -3'

941 sgNTC-2 Bottom oligo
942 5'- **AAA C**CC CAC CAA TAT CAG TAA TAC **C** -3'
943 sgIrf1 guide 1 Top oligo
944 5'- **CAC CG**T GGA AGC ACG CTG CTA AGC A -3'
945 sgIrf1 guide 1 Bottom oligo
946 5'- **AAA C**TG CTT AGC AGC GTG CTT CCA **C** -3'
947 sgIrf1 guide 2 Top oligo
948 5'- **CAC CG**C TGT AGG TTA TAC AGA TCA G -3'
949 sgIrf1 guide 2 Bottom oligo
950 5'- **AAA C**CT GAT CTG TAT AAC CTA CAG **C** -3'
951 sgStat1 guide 1 Top oligo
952 5'- **CAC CG**T ATC CTG TGG TAC AAC ATG C -3'
953 sgStat1 guide 1 Bottom oligo
954 5'- **AAA C**GC ATG TTG TAC CAC AGG ATA **C** -3'
955 sgStat1 guide 2 Top oligo
956 5'- **CAC CG**G CAA GCG TAA TCT CCA GGT A -3'
957 sgStat1 guide 2 Bottom oligo
958 5'- **AAA C**TA CCT GGA GAT TAC GCT TGC **C** -3'
959 sgIfngr1 guide 1 Top oligo
960 5'- **CAC CG**G GCT CGG AGA GAT TAC CCG A -3'
961 sgIfngr1 guide 1 Bottom oligo
962 5'- **AAA C**TC GGG TAA TCT CTC CGA GCC **C** -3'
963 sgIfngr1 guide 2 Top oligo
964 5'- **CAC CG**T ATA CCA ATA CGC AAA TAC C -3'
965 sgIfngr1 guide 2 Bottom oligo
966 5'- **AAA C**GG TAT TTG CGT ATT GGT ATA **C** -3'
967
968 **Library Cloning**
969 Six MetTag-LARRY-BC.ID libraries were generated via overhang PCR by amplifying the
970 region within the original pLARRY-eGFP plasmid containing random barcodes. Primers
971 were designed with overhangs containing: (1) a unique 6-nucleotide library identifier

(ID), (2) a chromium 10x capture sequence, and (3) BsmBI restriction sites flanking both ends of the barcode (synthesized by Sigma-Aldrich). Amplified barcode fragments were introduced into the pRG212 third-generation lentiviral plasmid using the NEB Golden Gate Assembly Kit (NEB, E1602S) at a 2:1 insert-to-vector molar ratio. The cloning reaction was transformed into Endura electrocompetent *E. coli* cells (Biosearch Technologies, 60242-1) and plated overnight on LB-AMP plates. $3x10^6$-$2x10^7$ CFU colonies were harvested by flushing prewarmed LB broth and cultured for 2 hours in liquid LB. sgRNA oligo pools were synthesized as oPools (IDT), containing BsmBI cloning compatible overhangs. The oligos were then annealed and introduced into the CROP-seq-V2.mCherry lentiviral plasmid using the NEB Golden Gate Assembly Kit as described above. Approximately 5x10^7 CFUs for OvCa library and 2x10^7 colonies for MetTag library were harvested for maxiprep.

For both LARRY barcode and CRISPR libraries, plasmids were purified using the ZymoPURE II Plasmid Maxiprep kit (Zymo Research, D4202). The MetTag-LARRY-BC.ID vector map and CROP-seq-V2.mCherry vector map will be made available on Addgene upon publication.

Plasmid Library Amplification and Diversity Validation

Plasmid DNA was amplified using two step PCR to first amplify and then add indexing sequences to libraries. First round PCR was conducted using custom P5 and P7 adapters with overhangs compatible with Nextera indexing primers, followed by cleanup with Agencourt AMPure XP beads (Beckman Coulter, NC9933872) at a 1.8x bead ratio to remove primers. Index PCR reaction was conducted as outlined in the Illumina 16S Metagenomic Sequencing Library Preparation manual (Illumina, Doc #15044223, page 11-12) using 2x KAPA HiFi HotStart ReadyMix (Roche, KK2601) and Nextera XT Index kit v2 primers (Illumina, FC-131-1001). Final indexed libraries were quantified via the Qubit HS assay kit. LARRY libraries were run on a Bioanalyzer instrument and sequenced on an Illumina MiSeq instrument. CRISPR libraries were run on TapeStation using the High Sensitivity D1000 assay (Agilent, 5067-5585, 5067-5594) and sequenced on a NovaSeq-X instrument. Demultiplexed fastq files were filtered for high quality reads, and the number of unique reads was quantified. For the CRISPR libraries,

1003 a customized script was used to estimate the percentage coverage based on the
1004 original guide RNA whitelist.
1005
1006 **Lentivirus Production and Target Cell Transduction**
1007 MetTag-LARRY-BC.ID, CROP-seq-V2.mCherry guide, or Lenti-Luciferase.P2A.Neo
1008 (Addgene # 105621), and second-generation lentiviral packaging plasmids were
1009 transfected into HEK293T cells along with the CalFectin transfection reagent
1010 (SignaGen, SL100478). Lentivirus was harvested after 72 hours and concentrated
1011 (Lenti-X Concentrator, Takara Bio, 631231). Concentrated lentivirus was added to target
1012 cells along with 8 ug/ml polybrene. To achieve low MOI for CRISPR screening
1013 experiments, ID8 p53$^{-/-}$ ovarian cancer cells were infected at a low multiplicity of
1014 infection (MOI) of 0.15, as calculated by the percentage of mCherry-positive cells 48
1015 hours post transduction. 48 hours post transfection, cells were selected with either
1016 G418 (pRG212-LARRY; Sigma-Aldrich, 4727878001) or puromycin (CROP-seq-
1017 V2.mCherry; Invivogen, ant-pr-1) for a minimum of 7 days.
1018
1019 **Genomic DNA (gDNA) Amplicon Library Preparation**
1020 Genomic DNA was extracted from cultured cells and digested tissues using either the
1021 Quick-DNA Midiprep Kit (Zymo Research, D4075) or the Quick-DNA Miniprep Plus Kit
1022 (Zymo Research, D4068), depending on the starting cell number. Extracted DNA yield
1023 was quantified via a NanoDrop spectrophotometer, and samples were normalized to the
1024 same, lowest input concentration prior to PCR. Two rounds of PCR amplification were
1025 performed on > 200 ng starting gDNA material. The first round was utilized for amplicon
1026 amplification with nested primers for 15-20 cycles using a high-fidelity hot start
1027 polymerase, followed by purification with a 1.8x bead-to-sample AMPure XP bead ratio.
1028 Eluted amplicon DNA was quantified using the Qubit high sensitivity (HS) assay kit
1029 (Thermo Fisher Scientific, Q33231) and concentrations normalized prior to indexing.
1030 Approximately 5 ng of DNA was carried into the index PCR rection, which was
1031 conducted similarly to the plasmid library construction protocol described above. Index
1032 products were purified using the same AMPure XP beads ratio to remove excess
1033 primers. Library quantity was assessed via the Qubit HS assay kit and analyzed on a

1034 TapeStation instrument using the High Sensitivity D1000 assay to confirm expected
1035 library size and distribution. LARRY gDNA libraries were sequenced in-house on an
1036 Illumina MiniSeq instrument (Mid output kit, 300 cycles) while CRISPR gDNA libraries
1037 (101 genes*10 guides per gene, 20 non targeting guides = 1,030 guides) were
1038 sequenced on a NovaSeq-X instrument. High quality reads were filtered and analyzed
1039 via two parallel approaches: LARRY barcode counts were extracted to quantify library
1040 batch identity (ID), while CRISPR libraries were processed using the MAGeCK pipeline
1041 to identify enriched or depleted guide RNAs. Primers used for amplification were as
1042 follows:
1043 LARRY Round 1 PCR REV, Tm: 55.9:
1044 5' – GTC TCG TGG GCT CGG AGA TGT GTA TAA GAG ACA GTG GGG AAT TTC TAC
1045 TCT TGT AGA TCG – 3'
1046 LARRY Round 1 PCR FWD Stagger, Tm: 59.0:
1047 5'-TCG TCG GCA GCG TCA GAT GTG TAT AAG AGA CAG CTT GCT AGG ACC GGC
1048 CTT AAA GC -3'
1049 CRISPR Round 1 PCR REV, Tm: 51.0:
1050 5' – GTC TCG TGG GCT CGG AGA TGT GTA TAA GAG ACA GTT CTT GGC TTT ATA
1051 TAT CTT GTG G– 3'
1052 CRISPR Round 1 PCR FWD Stagger, Tm: 53.0:
1053 5' – TCG TCG GCA GCG TCA GAT GTG TAT AAG AGA CAG CTC AAG TTG ATA ACG
1054 GAC TAG C– 3'
1055
1056 **PiggyBac Transposon Transfection**
1057 SpCas9 and CreERT2 coding sequences were cloned into PiggyBac transposon
1058 plasmids containing a hygromycin resistance cassette via Gateway cloning
1059 (ThermoFisher Scientific, 11791020 & 11789020). Target cells were plated in 6-well
1060 plates 24 hours prior to transfection. Five ug of the SpCas9 or 1 ug of CreERT2
1061 PiggyBac plasmid was co-transfected with 0.5 ug of Super PiggyBac Transposase
1062 (System Biosciences, PB210PA-1), along with the Calfectin transfection reagent. The
1063 transfection mixture was added to cells in a dropwise manner. 12-16 hours post
1064 transfection complete growth media was replenished. Forty-eight hours post

1065 transfection, cells were selected with hygromycin B (Corning, 30-240-CR) for a
1066 minimum of 10 days to enrich for successful transgene integrated cells.
1067
1068 **Cell Preparation for Single Cell RNA Sequencing**
1069 Naïve and tumor bearing mice were sacrificed via cervical dislocation six weeks
1070 following initial cancer cell injection. To collect peritoneal cells, 5 mL of cold 1xHBSS
1071 was injected intraperitoneally using a 25G needle, followed by lavage and peritoneal
1072 fluid retrieval using a 20G needle. Omenta were excised from the peritoneal cavity and
1073 examined under a dissecting microscope to confirm the presence of macroscopic
1074 metastases. Omental tissues were then minced and digested for 30 minutes at 37ºC in
1075 RPMI-1640 medium containing 0.4% collagenase type II (Gibco, 17101015), 50 ug/ml
1076 DNAseI, and 0.1% BSA. Following digestion, cell suspensions were passed through a
1077 70-uM strainer and washed with cold 1xPBS. Lavage, ascites, and omentum samples
1078 were resuspended in 1x RBC lysis buffer (BioLegend, 420301) to remove red blood
1079 cells. To prepare for single-cell analysis, omental samples were stained with ZombieRed
1080 (BioLegend, 423109) to exclude dead cells and sorted via FACS. Sorted cells were then
1081 prepared for 10X Genomics Chromium Single Cell Gene Expression analysis. A detailed
1082 protocol for sample multiplexing via hashtags can be found in the CITE-seq/cell hashing
1083 protocol on the CITE-seq website (https://cite-seq.com/wp-
1084 content/uploads/2019/02/cite-seq_and_hashing_protocol_190213.pdf). In brief, samples
1085 were first blocked with FcR Blocking Reagent (Miltenyi Biotec, 130-092-575) in 50 uL of
1086 cell staining buffer for 20 minutes on ice. Samples were then stained with TotalSeq™-A
1087 hashing antibodies obtained from BioLegend, including:
1088 M-HTO-1 (M1/42; 30-F11, 155801),
1089 M-HTO-2 (M1/42; 30-F11, 155803),
1090 M-HTO-3 (M1/42; 30-F11, 155805),
1091 M-HTO-4 (M1/42; 30-F11, 155807),
1092 M-HTO-5 (M1/42; 30-F11, 155809),
1093 M-HTO-6 (M1/42; 30-F11, 155811),
1094 M-HTO-7 (M1/42; 30-F11, 155813),
1095 M-HTO-8 (M1/42; 30-F11, 155815).

1096 Staining was performed for 25 minutes on ice, followed by three washes with staining
1097 buffer (decreasing EDTA concentration per wash) and loading onto a 10X Genomics
1098 Chromium Controller.
1099
1100 **scRNA-seq Library Preparation and Illumina Sequencing**
1101 Single-cell transcriptomic libraries were prepared as outlined in the Chromium Next
1102 GEM Single Cell 3' Reagents Kits v3.1 with Feature Barcoding technology kit manual.
1103 Kits necessary for transcriptome library preparation were: Chromium Next GEM Single
1104 Cell 3' GEM, Library & Gel Bead Kit v3.1, 4 rxns (10x Genomics, PN-1000128),
1105 Chromium Single Cell 3' Feature Barcode Library Kit, 16 rxns (10x Genomics, PN-
1106 1000079), Chromium Next GEM Chip G Single Cell Kit, 16 rxns (10x Genomics, PN-
1107 1000127), and Single Index Kit T Set A, 96 rxns (10x Genomics, PN-1000213).
1108 Hashtag libraries were prepared using the standard CITE-seq protocol (https://cite-
1109 seq.com/wp-content/uploads/2019/02/cite-seq_and_hashing_protocol_190213.pdf
1110). LARRY-BC.ID barcode libraries were constructed using a custom nested PCR
1111 protocol followed by indexing. Primers required for LARRY-BC.ID library preparation
1112 included:
1113 Round 1 PCR FWD, Tm: 61.0
1114 5' – *GCA GCG TCA GAT GTG TAT AAG AGA CAG* – 3'
1115 Round 1 PCR REV: 45.0
1116 5' – <u>CCT TGG CAC CCG AGA ATT CCA aat ttc tac tct tgt aga t</u> – 3'
1117 Index PCR FWD, Tm: 61.0
1118 5' – AAT GAT ACG GCG ACC ACC GAG ATC TAC ACT CGT CG*G CAG CGT CAG ATG*
1119 *TGT ATA AGA GAC AG* – 3'
1120 Index PCR REV (ADT-RPI-1), Tm 61.0:
1121 5' – CAA GCA GAA GAC GGC ATA CGA GAT CGT GAT GTG ACT GGA GTT <u>CCT TGG</u>
1122 <u>CAC CCG AGA ATT CCA</u> – 3'
1123 *{Partial Read 1N;* LARRY transcript (lowercase), <u>P7 adaptor</u>*,* RPI1 **index***}*
1124
1125 The quality and quantity of the three individual libraries (transcriptome, HTO, and
1126 LARRY) were assessed via Qubit and TapeStation prior to sequencing. Libraries were

pooled for sequencing on an Illumina NovaSeq X Plus platform with paired end reads (PE150).

scRNA-seq Data Analysis

Raw fastq files generated from the sequencing runs (mRNA, HTO, LARRY outputs) were processed through the 10x Genomics CellRanger pipeline v.7.2 to generate count matrices. Gene expression (mRNA) reads were aligned to a custom mouse reference genome containing fluorescent marker transcripts (mm10_3.0.0_FPs). Data from two different chromium 10x lanes, ascites lane and omentum lane, were merged using the SCT-normalized dataset integration method. Details related to integration steps can be found at: https://satijalab.org/seurat/articles/. In brief, individual lane single cell data was normalized for HTO (HTOdemux) followed by SCTransform prior to integration. Downstream analyses including dimensional reduction via principal component analysis (PCA), clustering and UMAP embedding, and differential gene expression (DEG) analysis were performed in RStudio under the Seurat package (v4.0)[18]. Cell type identities were assigned based on cluster marker genes. Subcluster level labels indicating different cellular statuses were determined through a combination of cluster marker genes and examining enriched pathways. RNA velocity analysis was performed in Python using scVelo and CellRank. Loom files were generated for each lane and merged, followed by Seurat object conversion to H5AD format. Metadata containing clustering and HTO information was integrated into the SCANPY anndata object. More details on the CellRank method can be found at: https://cellrank.readthedocs.io/en/latest/index.html. NicheNetR and CellChat were performed in RStudio. Sender and receiver cell types were selected prior to NicheNetR analysis. scRNA-seq expression data was analyzed using the Wilcoxon rank sum test either through the direct function wilcox.test() when assigning custom module scores or through the FindMarkers() function as part of the standard DEG analysis. Adjusted p values <0.05 were considered significant. Over-representation analysis (ORA) was performed on a filtered list of upregulated or downregulated genes from DEG analysis and the ReactomePA and clusterProfiler RStudio packages. org.Mm.eg.db package was used to convert genes to Entrez ID symbols. Adjusted p values <0.05 and log fold

1158 change > (+/-) 0.25 were considered significant. ORA uses Fisher's exact test to
1159 determine enriched gene sets. For Single Cell Gene Set Enrichment Analysis
1160 (ssGSEA), we utilized the Escape R package[19].
1161
1162 **Flow cytometry**
1163 Samples were extracted and pre-processed similarly as the scRNA-seq samples.
1164 Following tissue digestion of lung or omentum tissues and RBC lysis, digested samples
1165 were washed in 1x Flow Staining Buffer (Tonbo Biosciences, TNB-4222-L500). For
1166 viability assessment, cells were incubated with ZombieAqua Fixable Viability Kit
1167 (BioLegend, 423102) at a 1:750 dilution in 1xPBS for 20 minutes at room temperature.
1168 Following viability staining, cells were blocked with 1x FcR Blocking Reagent (Miltenyi
1169 Biotec, 130-092-575) to minimize nonspecific antibody staining. Cells were then stained
1170 with a combination of the following fluorochrome-conjugated surface antibodies: Pacific
1171 Blue™ anti-mouse CD45 (BioLegend, 157211, S18009F), APC/Fire™ 750 anti-mouse
1172 CD3 (BioLegend, 100247, 17A2) or PE/Cyanine7 anti-mouse CD3 (BioLegend, 100219,
1173 17A2), PE anti-TREM-2 (BioLegend, 824805, 6E9), APC anti-mouse CCR5 (BioLegend,
1174 107011, HM-CCR5), Brilliant Violet 605™ anti-mouse/human CD11b (BioLegend,
1175 101237, M1/70), APC anti-mouse I-A-I-E (BioLegend, 107613, M5/114.15.2), Brilliant
1176 Violet 711™ anti-mouse CD4 (BioLegend, 100447, GK1.5), PE/Dazzle™ 594 anti-
1177 mouse NK-1.1 (BioLegend, 156517, S17016D) or PE anti-mouse NK-1.1 (BioLegend,
1178 156503, S17016D), Brilliant Violet 421™ anti-mouse PD-L1 (BioLegend, 124315,
1179 10F.9G2), PE/Cyanine7 anti-mouse CD8a (BioLegend, 100721, 53-6.7) or
1180 APC/Cyanine7 anti-mouse CD8a (BioLegend, 100713, 53-6.7), Brilliant Violet 785™
1181 anti-mouse F4/80 (BioLegend, 123141, BM8). Cancer cells harvested from culture were
1182 similarly stained with ZombieAqua, FcR blocked, and then incubated with IFNGR1
1183 Recombinant Rabbit Monoclonal Antibody FITC (Invitrogen, MA5-46853, 062) with the
1184 corresponding Rabbit IgG Isotype Control FITC, eBioscience™ (Invitrogen, 11-4614-
1185 80). Cells were then washed with staining buffer, followed by analysis on a Cytek
1186 Northern Lights flow cytometer. FCS files were exported and analyzed using FlowJo
1187 (BD Biosciences).
1188

1189 **Western Blotting**

1190 Cells were plated at a density of 250,000-500,000 cells per 10 cm dish for regular
1191 attachment plate experiments. For anoikis assays, 3x 6 wells per sample were seeded
1192 with 300,000 cells each. The next day, cells were either treated with vehicle (1xPBS) or
1193 100 ng/ml mouse recombinant IFNγ (PeproTech, AF-315-05-100UG). After treatment,
1194 cells were harvested, washed with 1xPBS, and lysed in M2 lysis buffer (50 nM Tris-HCl,
1195 pH 7.4, 150 mM NaCl, 1% Triton X-100, 0.5 mM EDTA) with 1x Protease/Phosphatase
1196 Inhibitor Cocktail (CST, 5872). Cells were lysed for 1 hour on ice before centrifugation at
1197 high speed to collect protein lysates. Protein quantity was deterimed using the Pierce™
1198 BCA Protein Assay Kit (Thermo Scientific, 23225). Protein lysate samples utilized for
1199 GBP-1 detection were resolved using 4-20% Mini-PROTEAN TGX Precast Protein Gels
1200 (Bio-Rad, 4561094). Other immunoblots were performed on fixed concentration using 8-
1201 10% SDS-polyacrylamide gels. All gel transfers were performed onto nitrocellulose
1202 membranes (Fisher Scientific, 45-004-075). Nitrocellulose membranes were blocked in
1203 5% BSA/1xTBST for 1 hour at room temperature, followed by primary antibody
1204 incubation overnight on a 4ºC shaker. The following day, blots were washed with
1205 1xTBST followed by incubation with rabbit or mouse-specific horseradish peroxidase
1206 (HRP)-conjugated secondary antibodies. Signals were developed with SuperSignal
1207 West Pico PLUS Chemiluminescent Substrate (Thermo Fisher Scientific, #34577) or
1208 SuperSignal West Femto Maximum Sensitivity Substrate (Thermo Fisher Scientific,
1209 #34094). Primary antibodies used for western blotting were:
1210 Beta-Actin (13E5) Rabbit mAb, CST #4970, 1:5,000 dilution
1211 GBP-1 Rabbit Polyclonal Ab, {Thermo, PA5-23509}, 1:1,000 dilution
1212 Cas9 (S. pyogenes) (7A9-3A3) Mouse mAb, CST #14697, 1:1,000 dilution
1213 IRF-1 (D5E4) XP® Rabbit mAb, CST #8478, 1:1,000 dilution
1214 Cre Recombinase (D7L7L) XP® Rabbit mAb, CST #15036, 1:1,000 dilution
1215 GAPDH (14C10) Rabbit mAb, CST #2118, 1:5,000 dilution
1216 Stat1 (D1K9Y) Rabbit mAb, CST #14994, 1:1,000 dilution
1217 p-Stat1 (Tyr701) (58D6) Rabbit mAb #9167, 1:1,000 dilution
1218 Cleaved Caspase-3 (Asp175) Rabbit Ab #9661, 1:750 dilution
1219 SQSTM1/p62 Rabbit Ab #5114, 1:1,000 dilution

1220 STAT3 (124H6) Mouse mAb #9139, 1:1,000 dilution
1221 IDO (D8W5E) Rabbit mAb #51851, 1:1,000 dilution
1222 Phospho-STAT3 (Tyr705) (D3A7) XP® Rabbit mAb #9145, 1:1,000 dilution
1223 Vinculin (E1E9V) XP® Rabbit mAb #13901, 1:5,000 dilution
1224 Anti-rabbit IgG, HRP-linked Ab, CST #7074, 1:5,000 dilution
1225 Anti-mouse IgG, HRP-linked Ab, CST #7076, 1:5,000 dilution
1226

1227 **Clinical dataset mining**

1228 Patients were stratified into IFNGR1 high and IFNGR1 low expression groups and
1229 survival curve was generated using Kaplan-Meier Plotter (KMplotter,
1230 https://www.kmplot.com). This database includes 1816 samples primarily from
1231 GSE9891 and TCGA[32]. Correlation curves were drawn in RStudio upon downloading
1232 the TCGA-OV patient dataset[56] and calculating IFNγ, dormancy, and pro-survival
1233 scores. Patient scRNA-seq RDS file was obtained from Mendeley Data[57]
1234 (https://doi.org/10.17632/rc47y6m9mp.1) and contained 14 patient samples including
1235 PBMCs, lymph nodes, primary tumor, metastasis, and malignant ascites. The RNA data
1236 was re-normalized and analyzed using the Seurat package in RStudio in similar ways to
1237 the murine scRNA-seq dataset described above.
1238

1239 **Quantitative Reverse Transcriptase (RT) PCR**

1240 The IFNγ treatment time course was performed in 12 well plates. After seeding 1.0x105
1241 cells per well, wells were treated with 100 ng/ml IFNγ for 0 hours (PBS control), 4 hours,
1242 8 hours, or 24 hours. Total cell RNA was extracted from cells using the Direct-zol RNA
1243 Miniprep kit with TriReagent (Zymo Research, R2051-A) following the manufacturer
1244 protocol. One microgram of total RNA was used for reverse transcription to synthesize
1245 single stranded cDNA using the iScript™ Reverse Transcription Supermix for RT-qPCR
1246 (Bio-Rad, 1708840). qPCR reactions were performed on a Bio-Rad CFX Opus
1247 instrument with SsoAdvanced Universal SYBR Green Supermix (Bio-Rad, 1725270).
1248 Data analysis was performed using the CFX Maestro Software. Cq values were used to
1249 calculate relative gene expression levels. In brief, calculations were based on the $2^{-\Delta\Delta CT}$
1250 method with housekeeping genes serving as internal controls and fold change was

1251 calculated by normalizing to the zero-hour treatment timepoint Cq values. Statistical
1252 analyses and plots were generated in GraphPad Prism. RT-qPCR primers used were as
1253 follows:
1254 Beta-actin (Mouse) Forward primer TM: 57.6
1255 5'- GGC TGT ATT CCC CTC CAT CG -3'
1256 Beta-actin (Mouse) Reverse primer TM: 55.9
1257 5'- CCA GTT GGT AAC AAT GCC ATG T-3'
1258 GAPDH (Mouse) Forward primer TM: 59.8
1259 5'- CAT CAC TGC CAC CCA GAA GAC TG -3'
1260 GAPDH (Mouse) Reverse primer TM: 61.6
1261 5'- ATG CCA GTG AGC TTC CCG TTC AG -3'
1262 Gbp2b (Mouse) Forward primer TM: 58.5
1263 5'- ATC TGC TCA TTG CTC AGA CTT ACT GG -3'
1264 Gbp2b (Mouse) Reverse primer TM: 57.4
1265 5'- AAG TAT TTT CTC AGC ATC ACT TCA GCC -3'
1266 Irf1 (Mouse) Forward primer TM: 60.4
1267 5'- ACC AAA TCC CAG GGC TGA TCT GG -3'
1268 Irf1 (Mouse) Reverse primer TM: 58.3
1269 5'- GAA GTT TGC CTT CCA TGT CTT GGG-3'
1270 Stat1 (Mouse) Forward primer TM: 55.1
1271 5'- GCT GCC TAT GAT GTC TCG TTT -3'
1272 Stat1 (Mouse) Reverse primer TM: 55.2
1273 5'- TGC TTT TCC GTA TGT TGT GCT -3'
1274 Marco (Mouse) Forward primer TM: 61.1
1275 5'- ATC CAC CTG ATC CTG CTC ACG G -3'
1276 Marco (Mouse) Reverse primer TM: 60.8
1277 5'- CAC TGC AGC GAG AAG AAG GGC -3'
1278 Slfn1 (Mouse) Forward primer TM: 60.9
1279 5'- AGG GAA AGG TCA AGG CTC ACA TTA AAA ATC C -3'
1280 Slfn1 (Mouse) Reverse primer TM: 60.1
1281 5'- AGG CTT CCC AAC AGA GAC ATC TGG -3'

1282

1283 **Anoikis Assays**

1284 Cancer cells ($1x10^4$) were seeded into 96-well ultra-low attachment (ULA) plates
1285 (Corning, CLS7007) to mimic anchorage-independent conditions in the peritoneal cavity
1286 environment. After 24 hours, 100 ng/ml recombinant mouse IFNγ or vehicle control
1287 (1xPBS) was added to appropriate wells. Twenty-four hours after treatment (i.e. 48hr
1288 after start of culture), CellTiter-Glo Luminescent Cell Viability Assay reagent (Promega,
1289 G7570) was applied to every assay well, and plates were incubated for 20 min at room
1290 temperature. Luminescence, indicating cellular ATP levels, was measured using a
1291 Tecan plate reader instrument and analyzed using GraphPad Prism software.
1292 For macrophage coculture experiments, $1.0x10^4$ cancer cells were seeded together with
1293 $1.0x10^4$ macrophages per well in ULA plates. Macrophages were enriched from the
1294 peritoneal cavity of wild type female mice using the MojoSort Mouse F4/80 Positive
1295 Selection Kit (BioLegend, 480170), following manufacturer's protocol. After 48 hours of
1296 coculture, cell suspensions were harvested, pelleted, and incubated in TrypLE (Thermo
1297 Fisher Scientific, 12605028) for 10 minutes at 37 ºC to dissociate cell aggregates. Cell
1298 suspensions were passed through a 40-uM strainer before flow cytometric staining as
1299 described earlier.

1300

1301 **Colony Formation Assay**

1302 Two hundred ID8 $p53^{-/-}$ cells were plated onto 6 well plates at the start of the
1303 experiment. For wells treated with IFN-γ, 100 ng/ml IFN-γ was maintained throughout
1304 the 7-day colony formation assay period. Wells were washed with 1xPBS, fixed with
1305 methanol, and stained with crystal violet solution (0.5% w/v) at room temperature for 20
1306 minutes. Wells were then washed with deionized water and dried overnight. Colonies
1307 were counted and quantified in GraphPad Prism.

1308

1309 **Validation of Cre-based NicheTracing**

1310 HEK293T cells were transfected with a loxp-dsRED-loxp-eGFP Cre reporter construct
1311 (Addgene # 141148) and cocultured in a 1:1 ratio with Cre.ERT2 expressing ID8 $p53^{-/-}$
1312 or E0771 cell lines in the presence or absence of 2 uM 4-hydroxytamoxifen (4-OHT,

MedChemExpress, Cat # HY-16950). Seventy-two hours after plating, wells were assessed for GFP+ switched cells using a Nikon Ti2 microscope. For independent *in vivo* validation, E0771-Cre.ERT2 cells were injected into the retro-orbital sinus of Ai6 mice. One week post injection, three consecutive tamoxifen or corn oil control treatments were performed (75 mg/kg/dose) i.p.. Two weeks post cancer cell injection, mice were euthanized, perfused intracardially, and lungs were extracted for imaging and flow cytometry analysis. For the ovarian metastasis model, tamoxifen injections were administered in five consecutive doses, two weeks post ID8-Cre.ERT2 cell i.p. injection.

Data and Resource Availability

scRNA-seq data with LARRY barcode and HTO multiplexing was deposited at GEO: GSE302619 and will be made publicly available upon publishing. Human scRNA-seq data has been published elsewhere and is publicly available: GSE14764.
Code and any additional information required to reanalyze the data reported here can be requested from the lead contact.

REFERENCES

1. Gerstberger, S., Jiang, Q., and Ganesh, K. (2023). Metastasis. Cell *186*, 1564–1579. https://doi.org/10.1016/j.cell.2023.03.003.

2. Ritch, S.J., and Telleria, C.M. (2022). The Transcoelomic Ecosystem and Epithelial Ovarian Cancer Dissemination. Front. Endocrinol. *13*, 886533. https://doi.org/10.3389/fendo.2022.886533.

3. Motohara, T., Masuda, K., Morotti, M., Zheng, Y., El-Sahhar, S., Chong, K.Y., Wietek, N., Alsaadi, A., Carrami, E.M., Hu, Z., et al. (2019). An evolving story of the metastatic voyage of ovarian cancer cells: cellular and molecular orchestration of the adipose-rich metastatic microenvironment. Oncogene *38*, 2885–2898. https://doi.org/10.1038/s41388-018-0637-x.

4. Latifi, A., Luwor, R.B., Bilandzic, M., Nazaretian, S., Stenvers, K., Pyman, J., Zhu, H., Thompson, E.W., Quinn, M.A., Findlay, J.K., et al. (2012). Isolation and Characterization of Tumor Cells from the Ascites of Ovarian Cancer Patients: Molecular Phenotype of

Chemoresistant Ovarian Tumors. PLOS ONE *7*, e46858. https://doi.org/10.1371/journal.pone.0046858.

5. Ahmed, N., and Stenvers, K. (2013). Getting to Know Ovarian Cancer Ascites: Opportunities for Targeted Therapy-Based Translational Research. Front. Oncol. *3*. https://doi.org/10.3389/fonc.2013.00256.

6. Almeida-Nunes, D.L., Mendes-Frias, A., Silvestre, R., Dinis-Oliveira, R.J., and Ricardo, S. (2022). Immune Tumor Microenvironment in Ovarian Cancer Ascites. Int. J. Mol. Sci. *23*, 10692. https://doi.org/10.3390/ijms231810692.

7. Lane, D., Matte, I., Garde-Granger, P., Bessette, P., and Piché, A. (2018). Ascites IL-10 Promotes Ovarian Cancer Cell Migration. Cancer Microenviron. *11*, 115–124. https://doi.org/10.1007/s12307-018-0215-3.

8. Mustea, A., Pirvulescu, C., Könsgen, D., Braicu, E.I., Yuan, S., Sun, P., Lichtenegger, W., and Sehouli, J. (2008). Decreased IL-1 RA concentration in ascites is associated with a significant improvement in overall survival in ovarian cancer. Cytokine *42*, 77–84. https://doi.org/10.1016/j.cyto.2008.01.011.

9. Yamanoi, K., Matsumura, N., Murphy, S.K., Baba, T., Abiko, K., Hamanishi, J., Yamaguchi, K., Koshiyama, M., Konishi, I., and Mandai, M. (2016). Suppression of ABHD2 , identified through a functional genomics screen, causes anoikis resistance, chemoresistance and poor prognosis in ovarian cancer. Oncotarget *7*, 47620–47636. https://doi.org/10.18632/oncotarget.9951.

10. Lineage tracing on transcriptional landscapes links state to fate during differentiation | Science https://www.science.org/doi/10.1126/science.aaw3381.

11. Śliwa, A., Szczerba, A., Pięta, P.P., Białas, P., Lorek, J., Nowak-Markwitz, E., and Jankowska, A. (2024). A Recipe for Successful Metastasis: Transition and Migratory Modes of Ovarian Cancer Cells. Cancers *16*, 783. https://doi.org/10.3390/cancers16040783.

12. Schrijver, W.A.M.E., Selenica, P., Lee, J.Y., Ng, C.K.Y., Burke, K.A., Piscuoglio, S., Berman, S.H., Reis-Filho, J.S., Weigelt, B., van Diest, P.J., et al. (2018). Mutation Profiling of Key Cancer Genes in Primary Breast Cancers and Their Distant Metastases. Cancer Res. *78*, 3112–3121. https://doi.org/10.1158/0008-5472.CAN-17-2310.

13. Müller, V., and Pantel, K. (2004). Bone marrow micrometastases and circulating tumor cells: current aspects and future perspectives. Breast Cancer Res. *6*, 258–261. https://doi.org/10.1186/bcr942.

14. Sänger, N., Effenberger, K.E., Riethdorf, S., Van Haasteren, V., Gauwerky, J., Wiegratz, I., Strebhardt, K., Kaufmann, M., and Pantel, K. (2011). Disseminated tumor cells in the

bone marrow of patients with ductal carcinoma in situ. Int. J. Cancer *129*, 2522–2526. https://doi.org/10.1002/ijc.25895.

15. Ke, M., Sun, N., Lin, Z., Zhang, P., Hu, Y., Wu, S., Zheng, Z., Lu, Y., and Jin, H. (2023). SNHG18 inhibits bladder cancer cell proliferation by increasing p21 transcription through destabilizing c-Myc protein. Cancer Cell Int. *23*, 48. https://doi.org/10.1186/s12935-023-02887-w.

16. Fan, H., Yuan, J., Li, Y., Jia, Y., Li, J., Wang, X., and Li, X. (2021). MKL1-induced lncRNA SNHG18 drives the growth and metastasis of non-small cell lung cancer via the miR-211-5p/BRD4 axis. Cell Death Dis. *12*, 128. https://doi.org/10.1038/s41419-021-03399-z.

17. Dasgupta, A., Lim, A.R., and Ghajar, C.M. (2017). Circulating and disseminated tumor cells: harbingers or initiators of metastasis? Mol. Oncol. *11*, 40–61. https://doi.org/10.1002/1878-0261.12022.

18. Satija, R., Farrell, J.A., Gennert, D., Schier, A.F., and Regev, A. (2015). Spatial reconstruction of single-cell gene expression data. Nat. Biotechnol. *33*, 495–502. https://doi.org/10.1038/nbt.3192.

19. Borcherding, N., Vishwakarma, A., Voigt, A.P., Bellizzi, A., Kaplan, J., Nepple, K., Salem, A.K., Jenkins, R.W., Zakharia, Y., and Zhang, W. (2021). Mapping the immune environment in clear cell renal carcinoma by single-cell genomics. Commun. Biol. *4*, 122. https://doi.org/10.1038/s42003-020-01625-6.

20. Cellular barcoding to decipher clonal dynamics in disease | Science https://www.science.org/doi/10.1126/science.abm5874?url_ver=Z39.88-2003&rfr_id=ori:rid:crossref.org&rfr_dat=cr_pub%20%200pubmed.

21. CellRank for directed single-cell fate mapping | Nature Methods https://www.nature.com/articles/s41592-021-01346-6.

22. Yu, G., Wang, L.-G., Han, Y., and He, Q.-Y. (2012). clusterProfiler: an R Package for Comparing Biological Themes Among Gene Clusters. OMICS J. Integr. Biol. *16*, 284–287. https://doi.org/10.1089/omi.2011.0118.

23. Bahrami, S., and Drabløs, F. (2016). Gene regulation in the immediate-early response process. Adv. Biol. Regul. *62*, 37–49. https://doi.org/10.1016/j.jbior.2016.05.001.

24. Koivisto, E., Acosta, A.J., Moilanen, A.-M., Tokola, H., Aro, J., Pennanen, H., Säkkinen, H., Kaikkonen, L., Ruskoaho, H., and Rysä, J. (2014). Characterization of the Regulatory Mechanisms of Activating Transcription Factor 3 by Hypertrophic Stimuli in Rat Cardiomyocytes. PLOS ONE *9*, e105168. https://doi.org/10.1371/journal.pone.0105168.

1415 25. Zhao, J., Peng, H., Gao, J., Nong, A., Hua, H., Yang, S., Chen, L., Wu, X., Zhang, H., and
1416 Wang, J. (2021). Current insights into the expression and functions of tumor-derived
1417 immunoglobulins. Cell Death Discov. *7*, 148. https://doi.org/10.1038/s41420-021-
1418 00550-9.

1419 26. Mehta, A., and Merkel, O.M. (2020). Immunogenicity of Cas9 Protein. J. Pharm. Sci. *109*,
1420 62–67. https://doi.org/10.1016/j.xphs.2019.10.003.

1421 27. Li, W., Xu, H., Xiao, T., Cong, L., Love, M.I., Zhang, F., Irizarry, R.A., Liu, J.S., Brown, M.,
1422 and Liu, X.S. (2014). MAGeCK enables robust identification of essential genes from
1423 genome-scale CRISPR/Cas9 knockout screens. Genome Biol. *15*, 554.
1424 https://doi.org/10.1186/s13059-014-0554-4.

1425 28. Shultz, D.B., Sandhya Rani, M.R., Fuller, J.D., Ransohoff, R.M., and Stark, G.R. (2009).
1426 Roles of IKK-β, IRF1, and p65 in the Activation of Chemokine Genes by Interferon-γ. J.
1427 Interferon Cytokine Res. *29*, 817–824. https://doi.org/10.1089/jir.2009.0034.

1428 29. Fisch, D., Bando, H., Clough, B., Hornung, V., Yamamoto, M., Shenoy, A.R., and Frickel,
1429 E. (2019). Human GBP1 is a microbe-specific gatekeeper of macrophage apoptosis and
1430 pyroptosis. EMBO J. *38*, e100926. https://doi.org/10.15252/embj.2018100926.

1431 30. Tailor, D., Garcia-Marques, F.J., Bermudez, A., Pitteri, S.J., and Malhotra, S.V. (2023).
1432 Guanylate-binding protein 1 modulates proteasomal machinery in ovarian cancer.
1433 iScience *26*. https://doi.org/10.1016/j.isci.2023.108292.

1434 31. Honkala, A.T., Tailor, D., and Malhotra, S.V. (2020). Guanylate-Binding Protein 1: An
1435 Emerging Target in Inflammation and Cancer. Front. Immunol. *10*, 3139.
1436 https://doi.org/10.3389/fimmu.2019.03139.

1437 32. Győrffy, B. (2023). Discovery and ranking of the most robust prognostic biomarkers in
1438 serous ovarian cancer. GeroScience *45*, 1889–1898. https://doi.org/10.1007/s11357-
1439 023-00742-4.

1440 33. Kim, Y.-N., Koo, K.H., Sung, J.Y., Yun, U.-J., and Kim, H. (2012). Anoikis Resistance: An
1441 Essential Prerequisite for Tumor Metastasis. Int. J. Cell Biol. *2012*, 306879.
1442 https://doi.org/10.1155/2012/306879.

1443 34. Johnson, D.E., O'Keefe, R.A., and Grandis, J.R. (2018). Targeting the IL-6/JAK/STAT3
1444 signalling axis in cancer. Nat. Rev. Clin. Oncol. *15*, 234–248.
1445 https://doi.org/10.1038/nrclinonc.2018.8.

1446 35. Al Zaid Siddiquee, K., and Turkson, J. (2008). STAT3 as a target for inducing apoptosis in
1447 solid and hematological tumors. Cell Res. *18*, 254–267.
1448 https://doi.org/10.1038/cr.2008.18.

36. Qin, H., Yeh, W.-I., De Sarno, P., Holdbrooks, A.T., Liu, Y., Muldowney, M.T., Reynolds, S.L., Yanagisawa, L.L., Fox, T.H., Park, K., et al. (2012). Signal transducer and activator of transcription-3/suppressor of cytokine signaling-3 (STAT3/SOCS3) axis in myeloid cells regulates neuroinflammation. Proc. Natl. Acad. Sci. *109*, 5004–5009. https://doi.org/10.1073/pnas.1117218109.

37. Chemi, F., Mohan, S., Guevara, T., Clipson, A., Rothwell, D.G., and Dive, C. (2021). Early Dissemination of Circulating Tumor Cells: Biological and Clinical Insights. Front. Oncol. *11*. https://doi.org/10.3389/fonc.2021.672195.

38. Jin, S., Guerrero-Juarez, C.F., Zhang, L., Chang, I., Ramos, R., Kuan, C.-H., Myung, P., Plikus, M.V., and Nie, Q. (2021). Inference and analysis of cell-cell communication using CellChat. Nat. Commun. *12*, 1088. https://doi.org/10.1038/s41467-021-21246-9.

39. Chen, S., Saeed, A.F.U.H., Liu, Q., Jiang, Q., Xu, H., Xiao, G.G., Rao, L., and Duo, Y. (2023). Macrophages in immunoregulation and therapeutics. Signal Transduct. Target. Ther. *8*, 207. https://doi.org/10.1038/s41392-023-01452-1.

40. Ahmed, I., and Ismail, N. (2020). M1 and M2 Macrophages Polarization via mTORC1 Influences Innate Immunity and Outcome of Ehrlichia Infection. J. Cell. Immunol. *2*, 108–115. https://doi.org/10.33696/immunology.2.029.

41. O'Carroll, C., Fagan, A., Shanahan, F., and Carmody, R.J. (2014). Identification of a Unique Hybrid Macrophage-Polarization State following Recovery from Lipopolysaccharide Tolerance. J. Immunol. *192*, 427–436. https://doi.org/10.4049/jimmunol.1301722.

42. Browaeys, R., Saelens, W., and Saeys, Y. (2020). NicheNet: modeling intercellular communication by linking ligands to target genes. Nat. Methods *17*, 159–162. https://doi.org/10.1038/s41592-019-0667-5.

43. Pentcheva-Hoang, T., Egen, J.G., Wojnoonski, K., and Allison, J.P. (2004). B7-1 and B7-2 Selectively Recruit CTLA-4 and CD28 to the Immunological Synapse. Immunity *21*, 401–413. https://doi.org/10.1016/j.immuni.2004.06.017.

44. Butte, M.J., Keir, M.E., Phamduy, T.B., Sharpe, A.H., and Freeman, G.J. (2007). Programmed Death-1 Ligand 1 Interacts Specifically with the B7-1 Costimulatory Molecule to Inhibit T Cell Responses. Immunity *27*, 111–122. https://doi.org/10.1016/j.immuni.2007.05.016.

45. Iyer, S., Zhang, S., Yucel, S., Horn, H., Smith, S.G., Reinhardt, F., Hoefsmit, E., Assatova, B., Casado, J., Meinsohn, M.-C., et al. (2021). Genetically Defined Syngeneic Mouse Models of Ovarian Cancer as Tools for the Discovery of Combination Immunotherapy. Cancer Discov. *11*, 384–407. https://doi.org/10.1158/2159-8290.CD-20-0818.

46. Zheng, X., Wang, X., Cheng, X., Liu, Z., Yin, Y., Li, X., Huang, Z., Wang, Z., Guo, W., Ginhoux, F., et al. (2023). Single-cell analyses implicate ascites in remodeling the ecosystems of primary and metastatic tumors in ovarian cancer. Nat. Cancer *4*, 1138–1156. https://doi.org/10.1038/s43018-023-00599-8.

47. Patras, L., Shaashua, L., Matei, I., and Lyden, D. (2023). Immune determinants of the pre-metastatic niche. Cancer Cell *41*, 546–572. https://doi.org/10.1016/j.ccell.2023.02.018.

48. Peinado, H., Zhang, H., Matei, I.R., Costa-Silva, B., Hoshino, A., Rodrigues, G., Psaila, B., Kaplan, R.N., Bromberg, J.F., Kang, Y., et al. (2017). Pre-metastatic niches: organ-specific homes for metastases. Nat. Rev. Cancer *17*, 302–317. https://doi.org/10.1038/nrc.2017.6.

49. Hershey, B.J., Barozzi, S., Orsenigo, F., Pompei, S., Iannelli, F., Kamrad, S., Matafora, V., Pisati, F., Calabrese, L., Fragale, G., et al. (2023). Clonal cooperation through soluble metabolite exchange facilitates metastatic outgrowth by modulating Allee effect. Sci. Adv. *9*, eadh4184. https://doi.org/10.1126/sciadv.adh4184.

50. Wawrzyniak, P., and Hartman, M.L. (2025). Dual role of interferon-gamma in the response of melanoma patients to immunotherapy with immune checkpoint inhibitors. Mol. Cancer *24*, 89. https://doi.org/10.1186/s12943-025-02294-x.

51. Remsik, J., Tong, X., Kunes, R.Z., Li, M.J., Estrera, R., Snyder, J., Thomson, C., Osman, A.M., Chabot, K., Sener, U.T., et al. (2025). Interferon-γ orchestrates leptomeningeal anti-tumour response. Nature, 1–10. https://doi.org/10.1038/s41586-025-09012-z.

52. Jorgovanovic, D., Song, M., Wang, L., and Zhang, Y. (2020). Roles of IFN-γ in tumor progression and regression: a review. Biomark. Res. *8*, 49. https://doi.org/10.1186/s40364-020-00228-x.

53. Zheng, H., Guan, X., Meng, X., Tong, Y., Wang, Y., Xie, S., Guo, L., and Lu, R. (2023). IFN-γ in ovarian tumor microenvironment upregulates HLA-E expression and predicts a poor prognosis. J. Ovarian Res. *16*, 229. https://doi.org/10.1186/s13048-023-01286-z.

54. Reddy, S.U., Sadia, F.Z., Vancura, A., and Vancurova, I. (2024). IFNγ-Induced Bcl3, PD-L1 and IL-8 Signaling in Ovarian Cancer: Mechanisms and Clinical Significance. Cancers *16*, 2676. https://doi.org/10.3390/cancers16152676.

55. Ghisoni, E., Benedetti, F., Minasyan, A., Desbuisson, M., Cunnea, P., Grimm, A.J., Fahr, N., Capt, C., Rayroux, N., Carlo, F.D., et al. (2025). Myeloid cell networks govern re-establishment of original immune landscapes in recurrent ovarian cancer. Cancer Cell *0*. https://doi.org/10.1016/j.ccell.2025.07.005.

56. McLendon, R., Friedman, A., Bigner, D., Van Meir, E.G., Brat, D.J., M. Mastrogianakis, G., Olson, J.J., Mikkelsen, T., Lehman, N., Aldape, K., et al. (2008). Comprehensive genomic

characterization defines human glioblastoma genes and core pathways. Nature *455*, 1061–1068. https://doi.org/10.1038/nature07385.

57. Wang, X., and Zheng, X. (2022). scRNA-seq data in ovarian cancer. *1*. https://doi.org/10.17632/rc47y6m9mp.1.

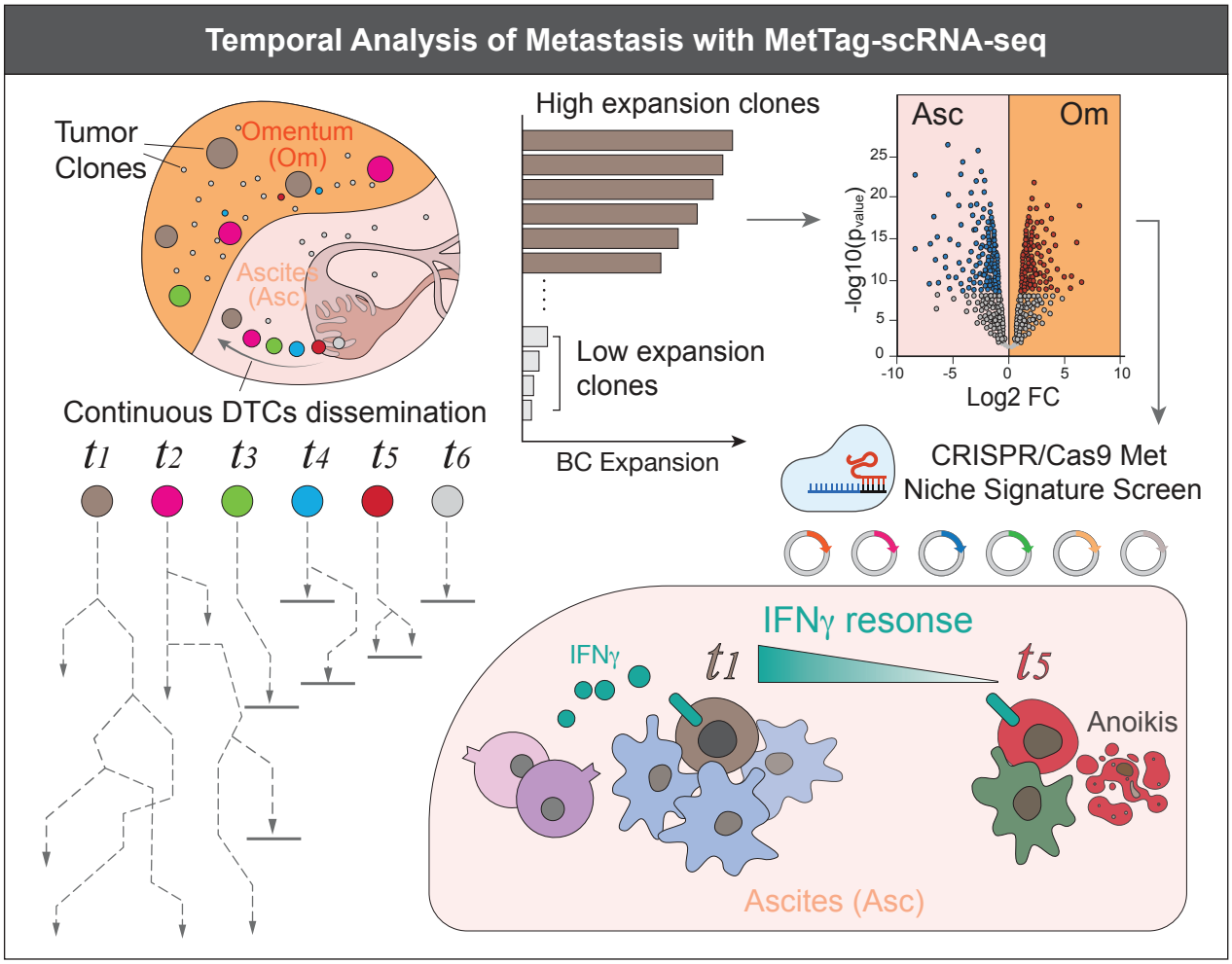

Graphical abstract

Figure 1:
Tracking Clonal Lineage in Ovarian Cancer Metastasis

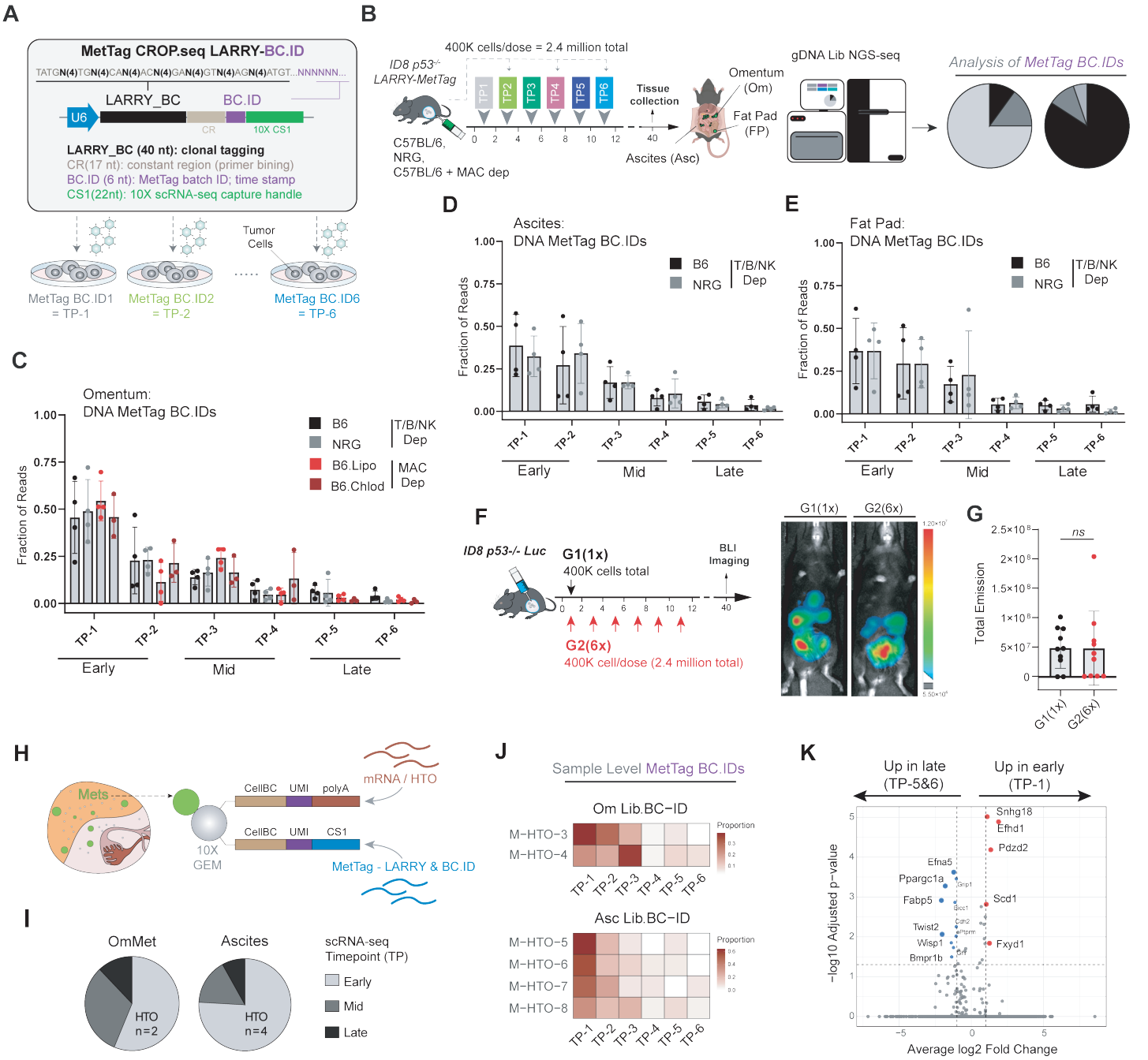

Figure 1: Tracking Clonal Lineage in Ovarian Cancer Metastasis
(**A**) Schematic depicting main elements of the MetTag library barcoding construct. (**B**) Schematic of injection and tissue collection timeline for the staggered injection experimental model using MetTag-barcoded ID8 ovarian cell lines. Schematic was partially created with BioRender.com. (**C**) Genomic DNA (gDNA)-level barcode distributions in the omentum graphed as frequency under WT, NRG, and MAC depletion conditions. (**D-E**) gDNA-level barcode distributions in ascites and pelvic fat pads under WT and NRG conditions. In (C-E) panels, BC.ID1 = TP-1, BC.ID2 = TP-2, BC.ID3 = TP-3, BC.ID4 = TP-4, BC.ID5 = TP-5, BC.ID6 = TP-6 for clarity. (**F**) Injection schema for comparing one-time (400,000 total, n = 10) cell dose and fractionated (2,400,000 total, n = 10) cell injections (left) and representative BLI images at endpoint (right). (**G**) Bar graph depicting total flux emission in each group at experimental endpoint. (**H**) Schematic of scRNA-seq experiment conducted using a reversed BC.ID injection order. LARRY barcodes are readily captured by Chromium 10x Feature Barcoding. (**I**) Pie charts of RNA-level barcode frequencies in each location grouped as early (BC.ID5, BC.ID6), mid (BC.ID4, BC.ID3), and late (BC.ID2, BC.ID1). (**J**) Heatmap of sample level barcode frequencies, BC.ID6 = TP-1, BC.ID5 = TP-2, BC.ID4 = TP-3, BC.ID3 = TP-4, BC.ID2 = TP-5, BC.ID1 = TP-6. (**K**) Volcano plot of DEGs between early and late timepoint barcoded cancer cells where threshold for significance was defined at p <0.05 and log2FC < -1.0 for downregulation or >1.0 for upregulation. Genes labeled are the top 30 genes based on significance. Data in Figure 1G was analyzed using a two-tailed Student's t test and graphed as mean with standard deviation (SD). In Figure 1K, the DEG table was generated using the Seurat FindMarkers() function and p values calculated via a Wilcoxon rank-sum test. For all Wilcoxon rank-sum tests, p values graphed represent the adjusted p value.

Figure 2:
Clonal Analysis Reveals Shared Evolutionary Path Towards Inflammatory Signature

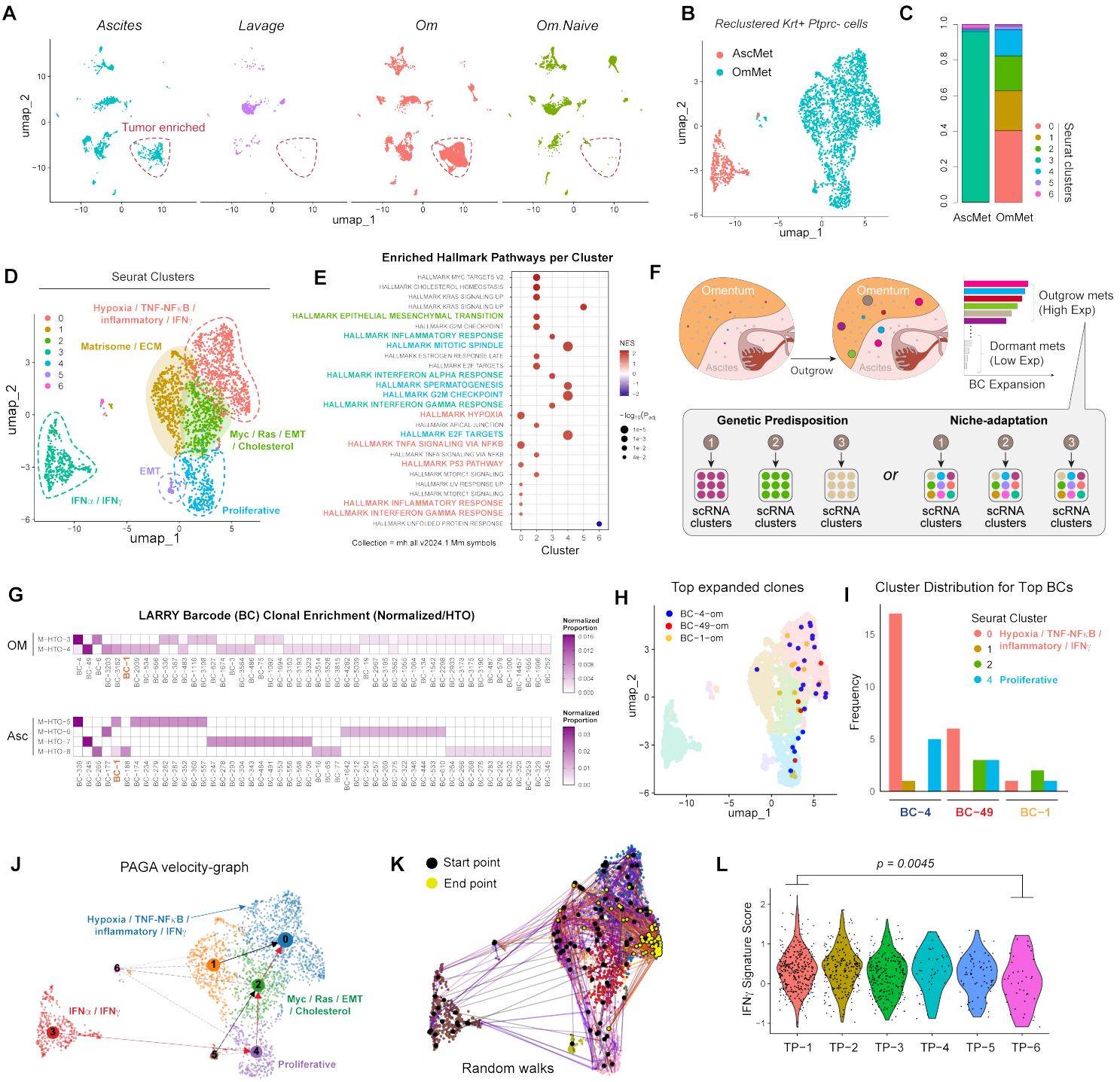

Figure 2: Clonal Analysis Reveals Shared Evolutionary Path Towards Inflammatory Signature
(**A**) Split UMAP depicting cluster distributions across the four experimental conditions and identifying cancer cell-enriched clusters in ascites and omentum. (**B**) Reclustered cancer cell UMAP colored by the two metastasis-bearing anatomical locations. (**C**) Stacked bar chart depicting the frequency of Seurat subclusters within each metastatic location. (**D**) Seurat cluster UMAP of reclustered cancer cells with transcriptional program labels. (**E**) Dot plot depicting Hallmark pathways across all subclusters used to define each cluster subset gene program in (D). (**F**) Schematic representation of the possible outcomes of LARRY clonal analysis based on transcriptome patterns of enriched clones. (**G**) Heatmap of normalized clonal LARRY barcode counts across the two anatomical locations and individual mice (HTOs). (**H**) UMAP overlay of top 3 expanded clones in the omentum. (**I**) Bar chart depicting the relative subcluster proportions present in each of the top 3 barcode clones. (**J**) scVelo-generated PAGA velocity graph indicating trajectory arrows and inferred cluster lineage. (**K**) scVelo and CellRank-based simulated path from start to endpoint clusters. (**L**) Violin plot depicting RNA-level contribution of each timepoint to the IFN-gamma signature. Data in Figure 2L was analyzed by first defining the IFN-gamma signature using canonical mouse genes, followed by directly applying the wilcox.test() function in Seurat to compare TP-1 and TP-6 expression.

Figure 3:

Activation of IFNγ Response in Ascites is Necessary for Successful Omental Colonization

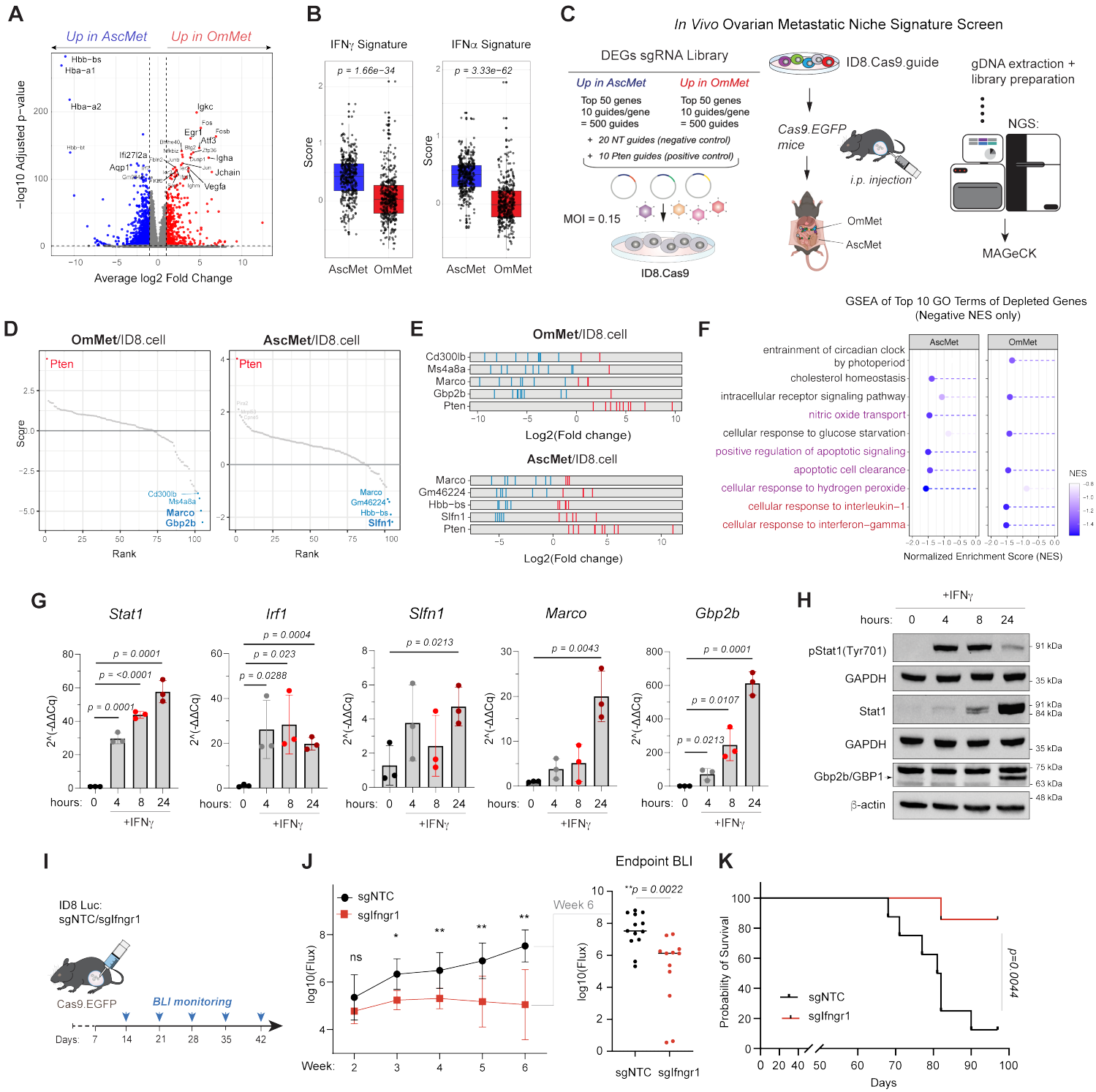

Figure 3: Activation of IFN-gamma Response in Ascites is Necessary for Successful Omental Colonization

(A) DEG-based volcano plot of gene expression differences between OmMet and AscMet, where threshold for significance was defined at p <0.05 and log2FC < -1.0 for downregulation or >1.0 for upregulation. (B) Boxplots comparing IFN signature modules between AscMet and OmMet. (C) Schematic describing in vivo ovarian metastatic niche signature screen. Partially created with BioRender.com. (D) In vivo CRISPR screen RankView plots generated using MAGeCKFlute. OmMet (n=5) and AscMet (n=4) samples were compared to the original pool of ID8 cells. (E) Ranks of individual sgRNAs targeting positive control Pten and depleted genes. (F) Lollipop plot of depleted pathways associated with depleted genes in Fig. 3E. (G) IFN-gamma treatment time course qPCR plots of select CRISPR hits and positive controls. (H) IFN treatment time course western blot probing for Stat1/pStat1 and GBP1. (I) Schematic of in vivo experimental metastasis study comparing sgNTC and sgIFNGR1.g1 groups. (J) Time course log10-transformed total emission/flux values (left). Two independent groups pooled; cohort 1 NTC n = 8, KO n = 7; cohort 2 NTC n = 5, KO n = 5. log10-transformed flux plot for week six with p value (right). (K) Kaplan Meier survival curve generated for cohort 1. Data in Figure 3B was analyzed by first defining IFN signatures, followed by applying wilcox-.test() in Seurat to compare AscMet and OmMet. CRISPR screen related data (3D-F) was first analyzed using MAGeCK.

Count summary, gRNA summary, and gene summary output files were loaded into RStudio to generate rankview plots using MAGeCKFlute. For Figure 3G, qPCR data was analyzed by averaging technical replicates for each biological replicate, followed by calculating dCq by normalizing target gene Cq to housekeeping gene control. Next, 2^(-ddCq) or fold change was calculated by normalizing the values to the zero hour (PBS) treatment samples and plotted in Prism GraphPad. Significance between groups was assessed using a two-tailed Student's t test and data was plotted as mean with standard deviation (SD). Data in figure 3J left panel was plotted as log transformed mean with 95% confidence interval (CI) and a two-tailed Student's t test was performed at each timepoint. Data in 3J right panel was plotted with median log transformed values.

Figure 4:
IFNγ Sensing Mediates Resistance to Anoikis and Activates Pro-survival Signaling

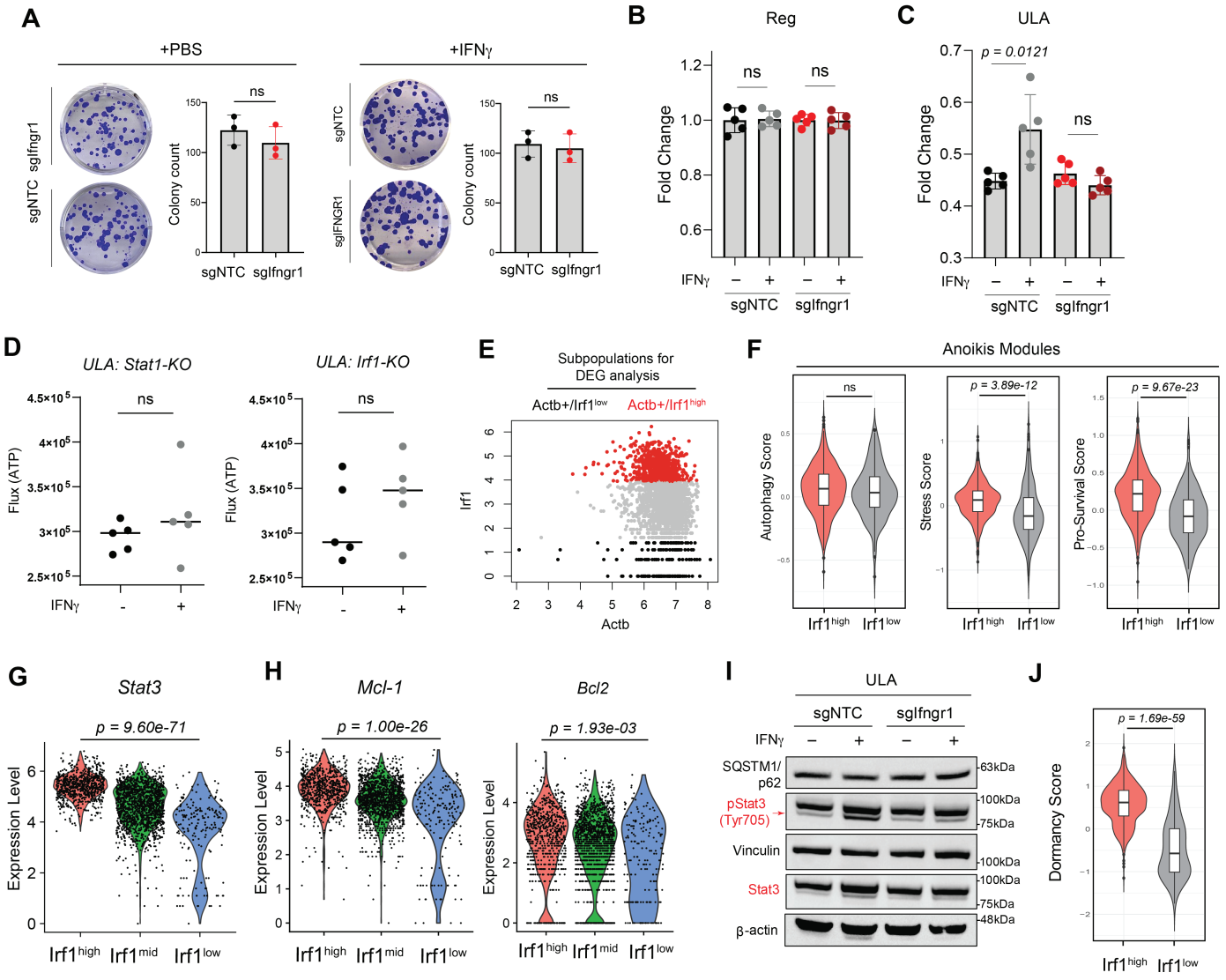

Figure 4: IFN-gamma Sensing Mediates Resistance to Anoikis and Activates Pro-survival Signaling
(**A**) Colony formation assay performed without (left) or with (right) 100 ng/ml IFN-gamma. (**B-C**) Cell-Titer Glo assay luminescence CTG values graphed as fold change for regular culture conditions (B) and ultra-low attachment conditions (C), with and without IFN-gamma treatment. Fold change was determined by normalizing each cell line's CTG value to the regular attachment, no IFN-gamma treatment condition. (**D**) CTG flux value dot plots for Stat1-KO and Irf1-KO cells under ultra-low attachment, with or without IFN-gamma treatment. (**E**) scRNA-seq based gating strategy used to identify Irf1-high and low cells for module scoring. (**F**) Violin plots for autophagy, stress, and pro-survival (anti-apoptotic) scores in Irf1-high vs. Irf1-low cells. Violin plots comparing *Stat3* (**G**), *Mcl-1*, and *Bcl2* (**H**) transcript levels between Irf1-high, mid, and low cells. (**I**) Western blot probing for Stat3 activation and SQSTM1 expression under ultra-low attachment conditions, with or without IFN-gamma treatments. (**J**) Violin plot of dormancy module comparing Irf1-high and low cells. CTG assay luminescence data (4B-4D) was analyzed in Prism using student's t test. Data in B and C was graphed as mean and standard deviation, data in D was graphed as median values. Anoikis and dormancy modules, along with *Stat3*, *Mcl-1*, and *Bcl2* transcript expression levels were compared between Irf1-high and Irf1-low cells by applying the wilcox.test() function in Seurat.

Figure 5:
Ascites and Omental TAMs Differ in Their Immunomodulatory Potential

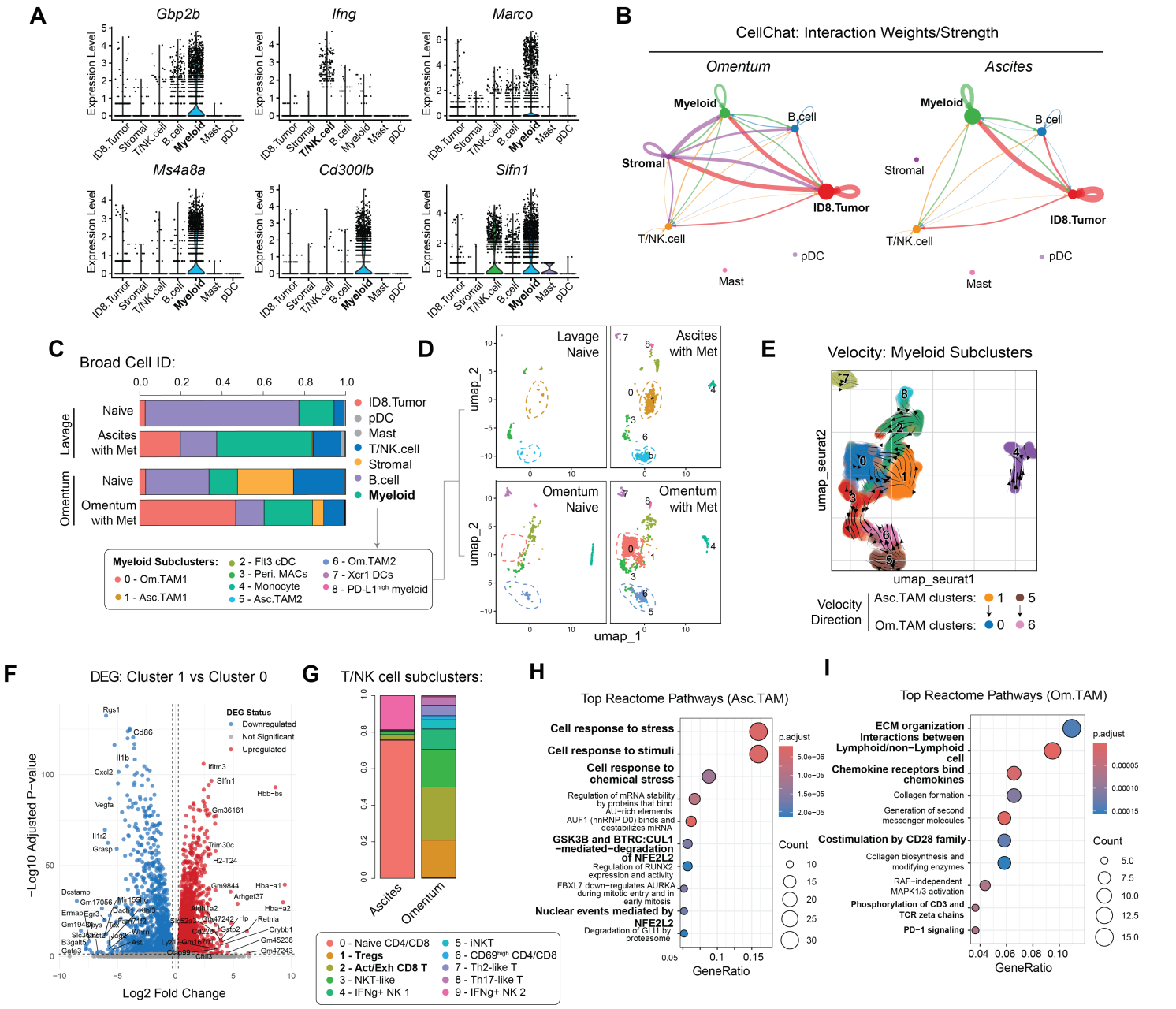

Figure 5: Ascites and Omental TAMs Differ in Their Immunomodulatory Potential
(**A**) Violin plots depicting CRISPR screen hits expression level across Broad cell ID categories (cell types). (**B**) CellChat-generated circus plots of interaction strengths between Broad cell ID categories in metastatic omentums (left) and ascites (right). (**C**) Stacked bar chart of cell type proportions across the four experimental groups. (**D**) UMAPs of reclustered myeloid cells, split by experimental condition. (**E**) scVelo RNA velocity plot showing arrows pointing from ascites TAMs (clusters 1 and 5) to omentum TAMs (clusters 0 and 6). (**F**) DEG volcano plot comparing gene expression differences between ascites TAM cluster 1 and omentum TAM cluster 0. (**G**) Stacked bar chart of subsetted T/NK cells comparing cell proportions in ascites and omentum. (**H-I**) ORA generated Reactome pathways enriched in ascital (left) and omentum-derived TAMs (right). Significance of DEGs in Figure 5F was evaluated by applying the FindMarkers() and Wilcoxon test in Seurat to compare ascites and omental *Cd68*^{high}/*Adgre1*^{high} macrophages.

Figure 6:
NicheTracing Identifies Ascites-derived TAMs as Pro-Metastatic Interactors

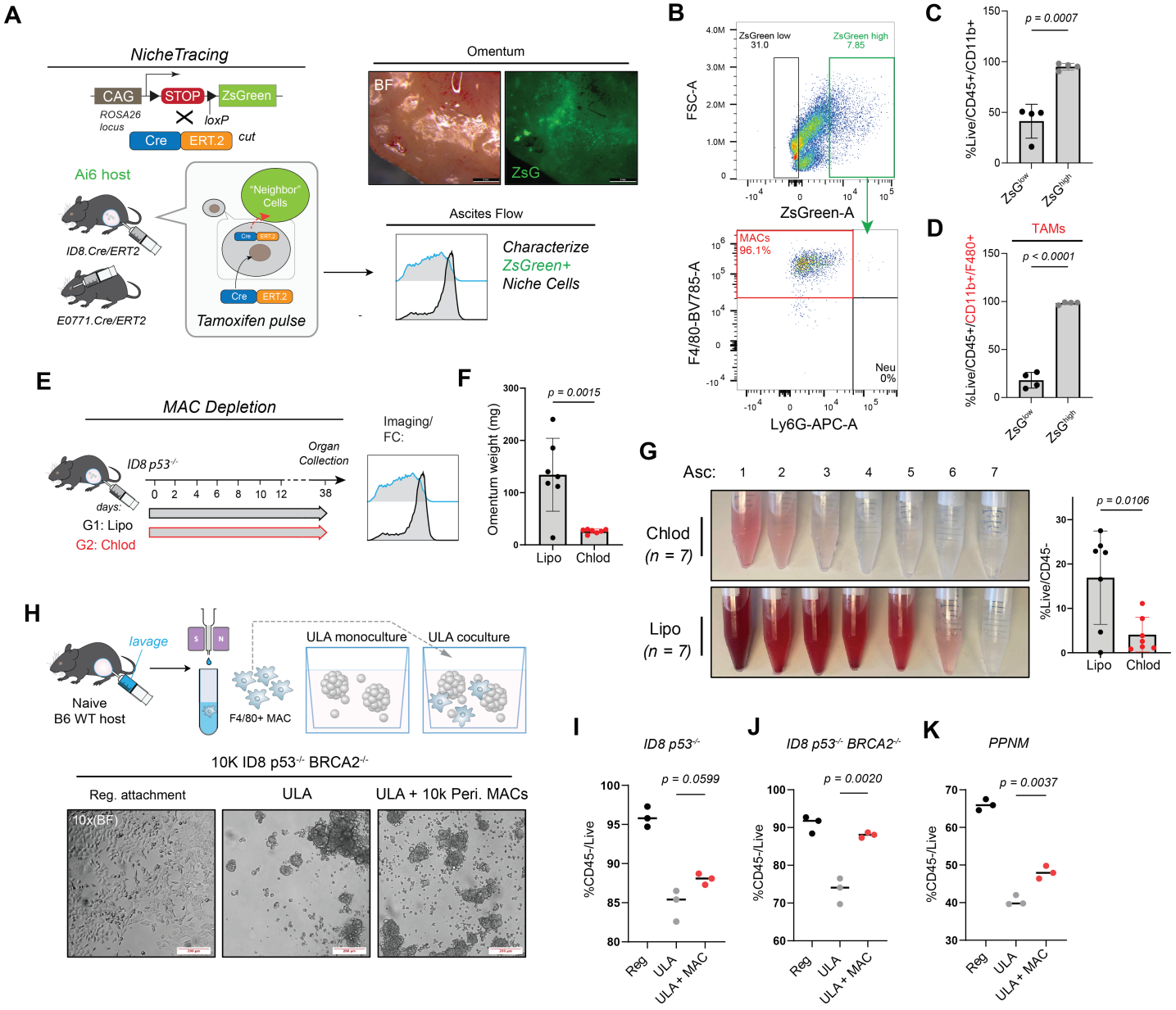

Figure 6: NicheTracing Identifies Ascites-derived TAMs as Pro-Metastatic Interactors
(**A**) Schematic describing the Cre-based NicheTracing labeling system where ID8 and E0771 cancer cells express Cre.ERT2 which transfers to neighboring RCL-ZsGreen niche cells. Upon nuclear entry of Cre.ERT2, labeled niche cells turn ZsGreen positive (ZsG+). (**B**) Representative gating strategy depicting the major cell population tagged with zsG. (**C-D**) Bar plots showing preference for F4/80+ macrophage labeling in ascites. (**E**) Liposomal chlodronate-based macrophage depletion strategy and timeline schematic with representative tissue images. n= 7 liposome control group and n = 7 chlodrosome treatment group. (**F**) Bar plot showing quantification of omental metastases via omental weight measurement at endpoint. (**G**) Images of ascites samples harvested at endpoint for flow cytometry analysis (left) and flow-based quantification of CD45 negative cells (right). (**H**) Schematic of macrophage-cancer cell coculture layout (top) and representative coculture images for one cell line (bottom). (**I-K**) Plots of percent CD45 negative cancer cell viability post coculture. Data in Figures 6C-D and 6F-6H was plotted as mean with SD and differences between groups were compared via a two-tailed unpaired Student's t test. Data in Figures 6I-K was similarly analyzed using a Student's t test and plotted with median values.

Figure 7:
Patient Ascites MAC/Tumor Interactions are Enriched for Tumor-supporting Pathways

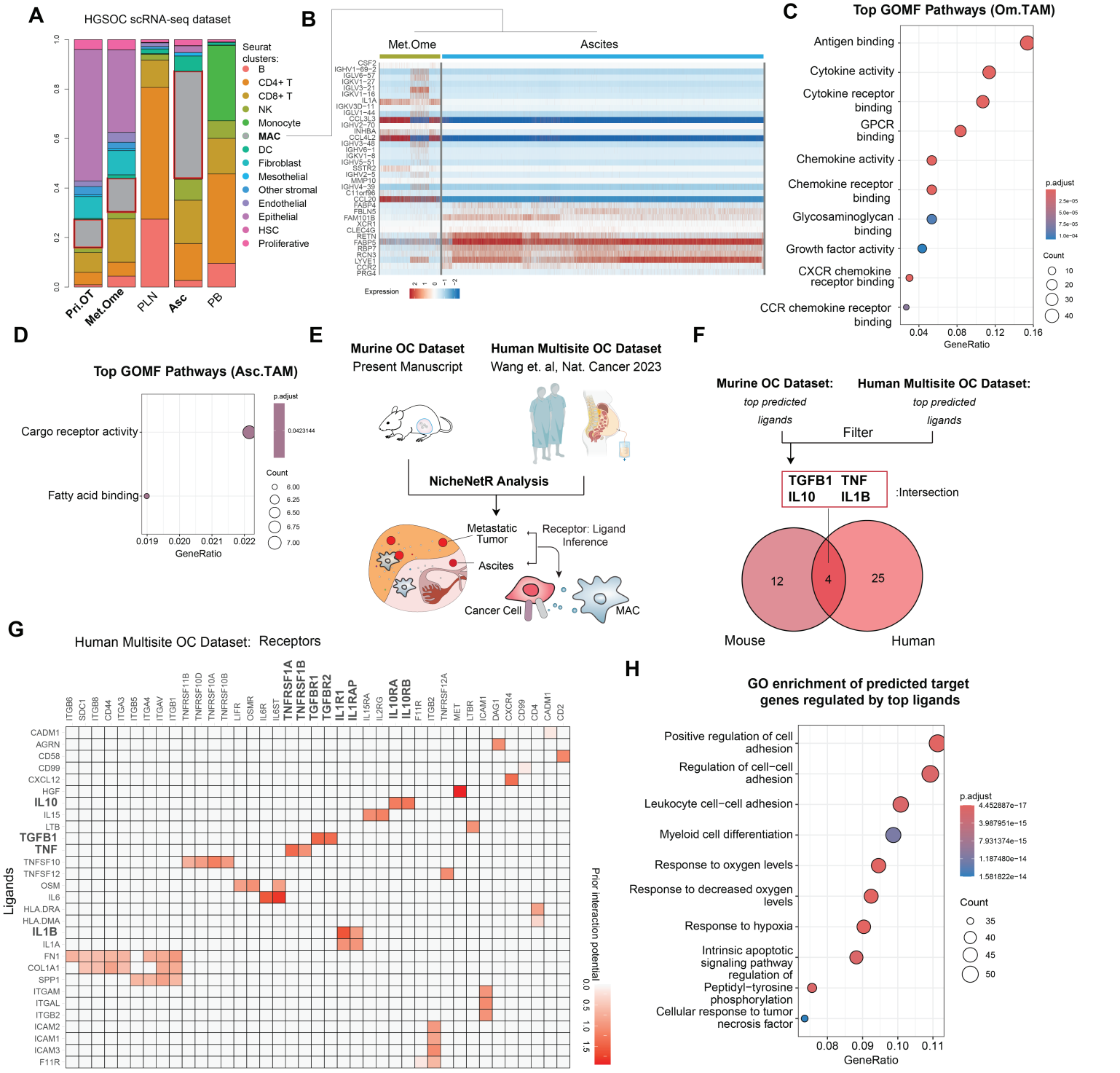

Figure 7: Patient Ascites MAC/Tumor Interactions are Enriched for Tumor-supporting Pathways
(**A**) Stacked bar chart of main cell type proportions captured in human scRNA-seq dataset across five anatomical locations, using main-type-2 annotation provided by publisher. (**B**) Heatmap depicting DEGs between Met.Ome and Ascites. (**C-D**) GO Molecular Function pathway level differences between omental MACs (C) and ascites MACs (D). (**E**) Schematic depicting NicheNetR analysis approach for finding top TAM ligands in both murine and human datasets. This panel was partially generated using BioRender.com. (**F**) Venn diagram of top NicheNet predicted ligands after filtering for robust expression and overlapping with top interactions in our murine dataset. (**G**) Heatmap showing top receptor-ligand interactions upregulated in patient ascites-MACs compared to metastases. (**H**) GO enrichment dotplot generated from the gene list containing top target genes in cancer cells that are predicted to respond to top ligands in the human dataset. Data in Figure 7B was analyzed using the FindMarkers() function in Seurat and Wilcoxon test to compare Asc and Met.Ome.